Capacitance Minimization and Constraint of CHB Power Electronic Transformer Based on Switching Synchronization Hybrid Phase-Shift Modulation Method of High Frequency Link

Yuzhuo Pan, Jiaxun Teng, Chen Yang, Zemin Bu, Baocheng Wang, Xin Li, and Xiaofeng Sun, *Member, IEEE*

***Abstract*—For the power electronic transformer based on cascaded H bridges with single inductor quad active bridge (SIQAB), this article proposes a submodule (SM) capacitance minimization scheme based on switching synchronization hybrid phase-shift modulation (SSHPSM) of high frequency link. Under SSHPSM, the primary side of SIQAB-stage operates in switched-capacitor mode to realize the automatic elimination of the second-order-frequency voltage ripple of SM capacitor without complex control, which helps to reduce the capacitance of SM and improve the power density of the system. The principle of low-frequency ripple transfer and cancellation is analyzed from the perspective of electric and magnetic coupling, and it shows that the scheme is still applicable under the influence of the nonideal factors. The power losses distribution and efficiency of dc–dc-stage and the capacitance constraints of SM are carried out. Furthermore, the operation feasibility of the proposed scheme in the case of the typical critical conditions are evaluated, including the low-frequency operation for motor drive and the fault ride-through ability of three-phase voltage asymmetry for grid-tied conditions. Finally, the proposed scheme is verified by simulation and experiment.**

***Index Terms*—Capacitance minimization, cascaded h bridge (CHB), power electronic transformer (PET), single inductor quad active bridge (SIQAB), synchronization modulation.**

NOMENCLATURE

PET	Power electronic transformer.
CHB	Cascaded H bridge.
QAB	Quad active bridge.
SIQAB	Single inductor quad active bridge.
HFL	High frequency link.
HFT	High frequency transformer.
CHB-QAB	Cascaded H bridges with quad active bridge.
CHB-SIQAB	Cascaded H bridges with single inductor quad active bridge.
SSHPSM	Switching synchronization hybrid phase-shift modulation.
MVac	Medium voltage ac.
LVdc	Low voltage dc.
SM	Submodule
u_{x}(x = a,b,c)	MVac voltage.
i_{x}(x = a,b,c)	MVac current.
U_{s}	Amplitude of MVac voltage.
${U_{\mathrm{s}}}^{+,-}$	Positive- and negative-sequential components of U_{s}.
I_{s}	Amplitude of MVac current.
${I_{\mathrm{s}}}^{+,-}$	Positive- and negative-sequential components of I_{s}.
i_{SMx}	SM charging current of phase-x.
$i_{\mathrm{SMx\text{-}dc}}$	Dc comment of i_{SMx}.
$i_{\mathrm{SMx\text{-}ac}}$	Ac comment of i_{SMx}.
$i_{\mathrm{Cx\text{-}ac}}$	Current of $i_{\mathrm{SMx\text{-}ac}}$ flowing into SM capacitor.
$i_{\mathrm{Qx\text{-}ac}}$	Current of $i_{\mathrm{SMx\text{-}ac}}$ flowing into SIQAB primary side port.
$i_{\mathrm{Qx\text{-}acy}}$	Current of $i_{\mathrm{Qx\text{-}ac}}$ flowing into other two phases.
i_{Cx}	Incompletely coupled ripple-current of SM capacitor current stimulated by three current sources.
C_{x}	SM capacitance of Phase-x.
u_{C}	Voltage of SM capacitor.
$u_{\mathrm{C\text{-}avg}}$	Average voltage of SM capacitor of three-phase.
$u_{\mathrm{Cx\text{-}avg}}$	Average voltage of SM capacitor of phase-x.
u_{LVdc}	LVdc voltage
P_{LVdc}	LVdc rated power.
u_{px}	HFT primary side voltage.
i_{px}	HFT primary side current.
$i_{\mathrm{p\text{-}dc}}$	Dc component of i_{px}.
$i_{\mathrm{px\text{-}ac}}$	Ac component of i_{px}.
u_{s}	HFT secondary side voltage.
i_{s}	HFT secondary side current.
L_{F}	Filtering inductance.

Manuscript received 1 September 2022; revised 9 December 2022; accepted 17 January 2023. Date of publication 23 January 2023; date of current version 10 March 2023. This work was supported in part by the Natural Science Foundation of Hebei Province under Grant E2021203162 and in part by Key Research and Development Program of Hebei Province under Grant 19214405D. Recommended for publication by Associate Editor C. Fernandez. *(Corresponding author: Xin Li; Xiaofeng Sun.)*

The authors are with the Key Laboratory of Power Electronics for Energy Conversion and Motor Drive of Hebei Province, Department of Electrical Engineering, Yanshan University, Qinhuangdao 066004, China (e-mail: 2976502354@qq.com; tengjiaxun@qq.com; 1097295810@qq.com; 18335388105@163.com; 199052257@qq.com; yddylixin@ysu.edu.cn; sxf@ysu.edu.cn).

Color versions of one or more figures in this article are available at https://doi.org/10.1109/TPEL.2023.3239164.

Digital Object Identifier 10.1109/TPEL.2023.3239164

L_{eq}	Sum of the external inductance and the equivalent leakage inductance.
L_{px}	External inductors under traditional scheme.
L_{Tx}	Leakage inductance of HFT primary side of SIQAB.
$\Delta L_{\mathrm{T1,2}}$	Difference between L_{Ta} and L_{Tb}, L_{Tc}.
L_{s}	External inductor of HFT secondary side of SIQAB.
ϕ_{px}	Phase angle of QAB primary side under traditional modulation method.
ϕ_{s}	Phase angle of QAB secondary side under traditional modulation method.
ϕ_{FB}	Phase angle of SIQAB primary side under SSHPSM method.
ϕ_{FBL}	Phase angle of SIQAB secondary side under SSHPSM method.
s_{i}	Switching function of SM.
g	Voltage modulation ratio.
$g^{+,-}$	Three-phase positive- and negative-sequence voltage modulation ratios.
ω	Fundamental angular frequency.
ω_{S}	High-frequency switching angular frequency of SIQAB.
f_{F}	Fundamental frequency.
f_{SM}	Switching frequency of CHB.
$f_{\mathrm{Q}}, f_{\mathrm{S}}$	Switching frequency of QHB and SIQAB.
φ	Power factor angle.
θ_{x}	Initial phase angle of phase-x.
${\theta_{\mathrm{x}}}^{+,-}$	Initial phase angles of the three-phase positive- and negative-sequence ${U_{\mathrm{s}}}^{+,-}$.
${\varphi_{\mathrm{x}}}^{+,-}$	Initial phase angles of the three-phase positive- and negative-sequence ${I_{\mathrm{s}}}^{+,-}$.
ε	SM capacitor voltage ripple coefficient.
Z_{Cx}	SM capacitor impedance.
Z_{LTx}	HFT leakage inductance impedance.
Z_{ex}	Equivalent input impedance of phase-x.
W_{px}	Primary side three port winding of SIQAB.
$W_{\mathrm{s1,23}}$	Secondary side winding of SIQAB.
$\Phi_{\mathrm{m1,23}}$	Magnetic flux covered by the primary winding.
$\Phi_{\mathrm{g1,23}}$	Magnetic flux flowing through the gap between the primary windings.
$R_{\mathrm{m1,23}}$	Magnetic reluctances corresponding to the $\Phi_{\mathrm{m1,23}}$.
$R_{\mathrm{g1,23}}$	Magnetic reluctances corresponding to the $\Phi_{\mathrm{g1,23}}$.
$R_{\delta\mathrm{1,23}}$	Leakage magnetic reluctances.
F_{px}	Magnetomotive force of the primary side winding.
$F_{\mathrm{s1,23}}$	Magnetomotive force of the secondary side winding.
N_{px}	Primary side winding turns.
ΔE_{SM}	Charging energy of SM capacitor.
D_{SM}	Duty cycle of the switch in the SM full-bridge.
V_{sw}	Switching time voltage.
$I_{\mathrm{swT,P}}$	Switching time current under traditional modulation and SSHPSM method.
$t_{\mathrm{ON,OFF}}$	Time intervals during switching ON and OFF.
T_{2F}	Second-order-frequency cycle.
$I_{\mathrm{rmsT,P}}$	Rms currents under traditional and modulation SSHPSM method.
R_{DS}	Conduction resistance.

I. Introduction

In recent years, cascaded H bridge power electronic transformer (CHB-PET) is researched deeply in the field of motor drive and smart grid as it is modular highly, easy to expand and friendly for redundant operation [1], [2], [3]. In 2009, single-phase CHB-PET was proposed to enable active management of distributed renewable energy resources, energy storage devices, and loads [4]. The single-phase CHB-PET consists a cascaded H bridge ac–dc rectifier, and a dual active bridge (DAB) converter with a high-frequency transformer (HFT), which the front end connects to the SM of the ac–dc rectifier and the output port is connected in parallel to form the low-voltage dc (LVdc) bus. X. Wang et al. [5] proposed a three-phase CHB-PET, as shown in Fig. 1(a). Li et al. [6] took the QAB converter as a basic module to provide a solution, as shown in Fig. 1(b), which can reduce the number of HFTs, and, which also maintain the merit of electromagnetic interference. The CHB-PET requires a larger capacitance to suppress the second-order-frequency voltage ripple in the submodule (SM) of the CHB-stage, which reduces the power density of the system, and increases the cost of the system [7]. Thus, reducing the capacitance of CHB-stage SM is of great significance to the practical engineering application of CHB-stage, and the main methods of capacitance reduction include hardware filter and software suppression.

The schemes of hardware filter include large size SM capacitance and adding *LC* secondary resonance filter [8], [9], [10]. These schemes are simple and effective; however, volume and cost will be increased. Software method can be realized by the following two method. 1) The third harmonic injection strategy is often adopted in modulation voltage of SM to eliminate the second-order-frequency harmonic of CHB-stage [11], [12]. However, the optimal amplitude and phase of the injected harmonic required to be calculated, which will consume a lot of controller resources. 2) The ripple-power transfer strategy is used to decouple the ripple-power from the SM capacitor based on SM cascaded dc–dc converter [6], [13], [14], [15]. However, to control the ripple currents or powers the regulator should be designed carefully and corresponding dynamics disturbance could not be canceled. Hu et al. [11] proposed a third harmonic injection method based on zero-sequence component of fundamental frequency to avoid overmodulation and minimize the capacitor voltage ripple. Hu et al. [12] further derived the optimal phase and amplitude of the third harmonic voltage to minimize the current stress and reduce the voltage ripple of the SM capacitor. Xiao et al. [13] proposed a ripple-power control loop of dc–dc-stage to suppress SM capacitor voltage ripple. In [14], the dual active bridge (DAB) transferred the second-order-frequency reactive power to the common LVdc bus and canceled it to eliminate the voltage ripple of the SM capacitor with negligible effect on the voltage ripple at LVdc link. Isobe et al. [15] proposed a control method of synchronous

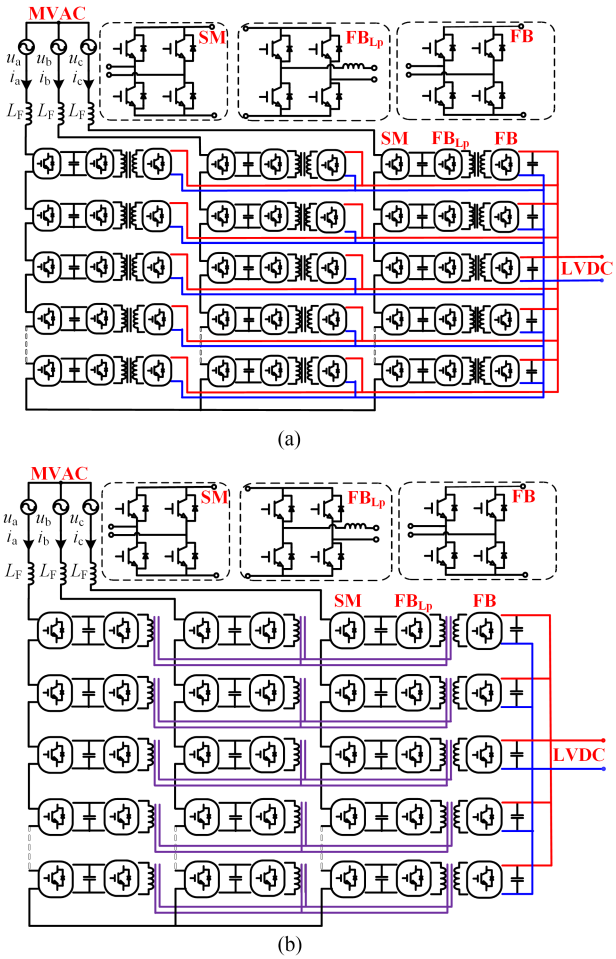

Fig. 1. Traditional CHB-PET topology. (a) CHB-DAB topology. (b) CHB-QAB topology.

instantaneous power of the ac–dc rectifier, and thereby the second-order-frequency component applied to the capacitors between the ac–dc and dc–dc converters could be canceled. The power decoupling control strategy achieved by the ripple-power control of dc–dc stage is also studied in [6], which can also eliminate the influence of asymmetric parameters.

This article proposes a capacitance minimization scheme to eliminate the second-order-frequency voltage ripple of the SM capacitor of the CHB with single inductor quad active bridge (CHB-SIQAB) scheme shown in Fig. 2, which is characterized by as follows.

1) The automatically transfer of ripple-current is based on synchronization modulation of primary side full bridge switches of SIQAB-stage and three-phase SM formed switched-capacitor circuits and the design of small leakage inductance of transformer primary sides, without additional hardware filtration, and complex control strategy.
2) The low-frequency ripple is eliminated based on the three-phase symmetry. Compared with the traditional large capacitance scheme, the SM capacitor volume is reduced by 85% and the cost is reduced by 85.6%.
3) The scheme is still applicable under some nonideal conditions including the influence of the nonideal switch synchronization signal caused by hardware factors and the leakage inductance inconsistency in HFT. It can still work well in the low-frequency operation for motor drive conditions and has the fault ride-through ability of three-phase voltage asymmetry for grid-tied conditions.

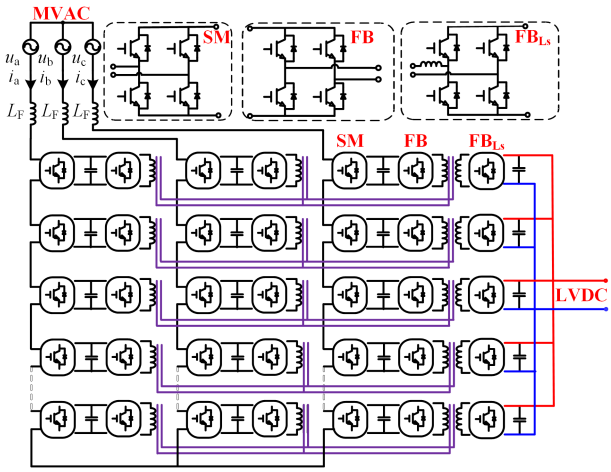

Fig. 2. CHB-SIQAB topology under the capacitance minimization scheme.

The rest of this article is organized as follows. In Section II, the traditional large capacitance scheme and the large capacitance constraint are given. In Section III, the capacitor minimization scheme is proposed, the principle of ripple transfer, and cancellation is analyzed and the system loss and capacitance minimization effect are also demonstrated. In Section IV, the influence on the characteristics of switched-capacitor circuits under the practical nonideal conditions is further analyzed. In Section V, the operation feasibility of the proposed scheme in the case of the typical critical conditions are also evaluated, including the low-frequency operation for motor drive conditions and the fault ride-through ability of three-phase voltage asymmetry for grid-tied conditions. In Section VI and VII, simulation and experimental results are provided to validate the theoretical analysis and control methods. Finally, Section VIII concludes this article.

II. Capacitance Constraint for CHB-PET Under Traditional Phase-Shift Control of QAB-Stage

A. Traditional Control Strategy of CHB-PET

The traditional CHB with quad active bridge (CHB-QAB) topology is shown in Fig 1(b), and its traditional control diagram, QAB circuit, equivalent model and modulation method are shown in Fig 3(a)–(d). Fig. 3(a) is the control diagram of CHB-stage in which the SM capacitor voltage average value $u_{\text{C-avg}}$ is taken as the feedback to stabilize SM capacitor voltage. Besides that, a SM capacitor voltage balancing strategy is added, where u_{C} is the SM capacitor voltage.

Fig. 3(b) shows the traditional phase-shift control diagram of the QAB-stage including the LVdc bus voltage outer loop and the power balancing loop, which regulates the power transferred from the primary side to the secondary side through different

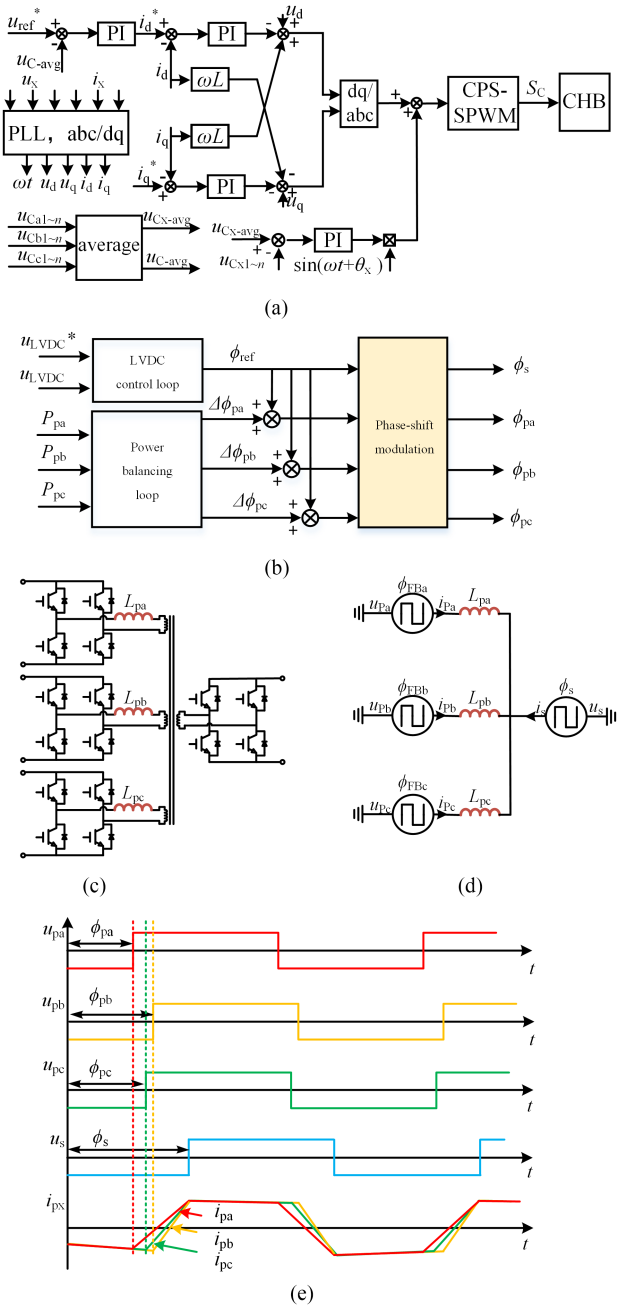

Fig. 3. Control and modulation strategy of traditional CHB-QAB. (a) CHB-stage control strategy. (b) QAB-stage control strategy. (c) QAB-stage circuit. (d) QAB-stage equivalent model. (e) Traditional modulation method.

phase shifts according to [16] and [17]

$$P = \frac{N u_{\mathrm{p}} u_{\mathrm{s}}}{2\pi f_{\mathrm{Q}} L_{\mathrm{eq}}} \phi_{\mathrm{px-s}} \left(1 - \frac{\phi_{\mathrm{px-s}}}{\pi}\right). \tag{1}$$

In (1), N is the transformer ratio, u_{p} and u_{s} are the primary and secondary side voltages of the transformer, respectively, f_{Q} is the switching frequency of QAB-stage. In high-power low frequency applications, the inductor cannot be provided by the leakage inductance, so the additional inductance needs to be added and L_{eq} is the sum of the external inductance and the equivalent leakage inductance. The QAB-stage circuit

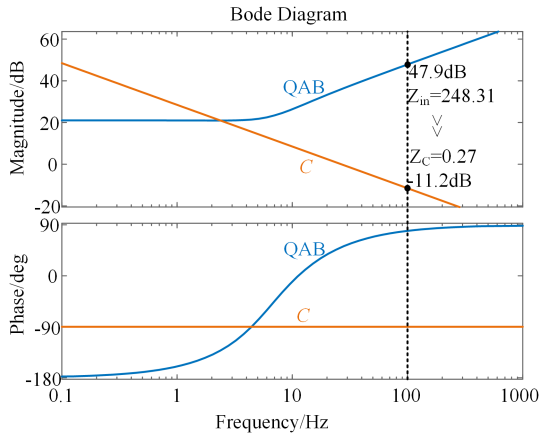

Fig. 4. Input impedance comparison between QAB-stage input impedance and the SM capacitance impedance.

and equivalent model under this control strategy are shown in Fig. 3(c) and (d), where u_{px} and i_{px} are the HFT voltages and currents, L_{pa}, L_{pb}, and L_{pc} are external inductors set on the primary sides of the HFT. The power flowing between primary and secondary ports is controlled by the phase-shift modulation, the diagram of which is shown in Fig. 3(e), where φ_{px} is the different phase-shift under the control strategy shown in Fig. 3(b).

B. Traditional Capacitance Constraint of SM

Under the traditional phase-shift modulation method shown in Fig. 3(b)–(e), the input impedance comparison between QAB-stage and SM capacitor at the second-order-frequency is shown in Fig. 4 under the operation conditions in Table IV. It can be seen that the QAB-stage input impedance at the second-order-frequency is greater than the impedance of the SM capacitance, so the second-order-frequency ripple-current is mainly absorbed by the SM capacitor and generates voltage ripple. In order to suppress the ripple within a certain range, the large SM capacitance is needed but it will increase the volume of the system and reduce the power density of the system. Alternatively, the ripple-power transfer strategy can be used to transfer the second-order-frequency ripple to the dc–dc-stage to decouple with SM capacitors according to [6], [13], [14], and [15] but it is usually complicated.

Without considering additional complex control, the capacitance constraint of the required large capacitance are as follows. The charging current of the SM is expressed as

$$\begin{aligned} i_{\mathrm{SMx}} &= s_{\mathrm{i}} \cdot i_{\mathrm{x}} \\ &= g \sin(\omega t + \theta_{\mathrm{x}}) \cdot I_{\mathrm{s}} \sin(\omega t - \varphi + \theta_{\mathrm{x}}) \end{aligned} \tag{2}$$

where i_{SMx} is the charging current of SM capacitor, s_{i} is the switching function of SM, $i_{\mathrm{x}}(t)$ is the phase-x current (x = a, b, c), g is the voltage modulation ratio, I_{s} is the phase-x current amplitude, ω and φ are fundamental angular frequency and power factor angle, θ_{x}(x = a, b, c) is the initial phase angle of each phase, where $\theta_{\mathrm{a}} = 0$, $\theta_{\mathrm{b}} = -2\pi/3$, $\theta_{\mathrm{c}} = 2\pi/3$. The i_{SMx} is further expressed, as shown in (3), which contains

TABLE I
SM CAPACITANCE OF CHB-STAGE AT DIFFERENT POWER LEVELS

Reference	The CHB-PET power rating (P_{base}:1MW)	Grid Voltage (V_{base}:10kV)	SM voltage (V_{base}:1kV)	SM capacitance (C_{base}:1mF)
[17]	0.5p.u.	0.33p.u.	1p.u.	3.3p.u.
[18]	1p.u.	1p.u.	0.8p.u.	2.5p.u.
[19]	2.25p.u.	1p.u.	3p.u.	4.7p.u.

the dc component $i_{\mathrm{SMx\text{-}dc}}$ and the second-order-frequency ac component $i_{\mathrm{SMx\text{-}ac}}$, where the specific expression of $i_{\mathrm{SMx\text{-}ac}}$ is shown in (4)

$$\begin{aligned} i_{\mathrm{SMx}} &= i_{\mathrm{SM\_dc}} + i_{\mathrm{SMx\_ac}} \\ &= \frac{I_s g}{2}\cos\varphi - \frac{I_s g}{2}\cos\left(2\omega t - \varphi + 2\theta_x\right) \end{aligned} \tag{3}$$

$$\begin{cases} i_{\mathrm{SMa\_ac}} = -\frac{I_s g}{2}\cos\left(2\omega t - \varphi\right) \\ i_{\mathrm{SMb\_ac}} = -\frac{I_s g}{2}\cos\left(2\omega t - \varphi + 2\pi/3\right) \\ i_{\mathrm{SMc\_ac}} = -\frac{I_s g}{2}\cos\left(2\omega t - \varphi - 2\pi/3\right). \end{cases} \tag{4}$$

The three-phase symmetrical ripple-current $i_{\mathrm{SMx\text{-}ac}}$ shown in (4) will cause voltage ripple of SM capacitor, which need to be absorbed by a larger capacitance, so the constraint of the CHB-stage SM capacitance can be obtained from [14]

$$C \geq \frac{I_s g}{4\pi f_F \varepsilon u_C}. \tag{5}$$

In (5), εu_c is the allowable peak-to-peak value of voltage ripple of SM capacitor, ε is the SM capacitor voltage ripple coefficient, and f_F is the fundamental frequency. In practical applications, the large capacitance limits the improvement of power density of the system. Table I shows the SM capacitance as per unit value of traditional CHB-PET at different power levels under the traditional control strategy.

III. CAPACITANCE MINIMIZATION SCHEME BASED ON SWITCHING SYNCHRONIZATION HYBRID PHASE-SHIFT MODULATION OF SIQAB-STAGE

A. Switching Synchronization Hybrid Phase-Shift Modulation of SIQAB-Stage

For the purpose of low-capacitance minimization design of CHB-PET, the capacitance minimization scheme based on switching synchronization hybrid phase-shift modulation (SSHPSM) method is proposed in this article. The CHB-stage still adopts the control strategy shown in Fig. 3(a), the change of dc–dc-stage circuit in Fig. 2 is shown in Fig. 5(b), and its equivalent circuit is shown in Fig. 5(c). There are no external inductors on the primary side of the transformer, and only the external inductor L_s on the secondary side of the HFT achieve power transfer. This structure is defined as SIQAB, and its control strategy block diagram is shown in Fig. 5(a). Only LVdc control loop is adopted, and the SSHPSM modulation method is shown in Fig. 5(d). Under SSHPSM, the phase-angles of the three full-bridges modulation signals on the primary side are all ϕ_{FB}, and the phase angle on the secondary side is ϕ_{FBL}, hence, the phase-shift angle is $\phi = \phi_{\mathrm{FB}} - \phi_{\mathrm{FBL}}$, the active power

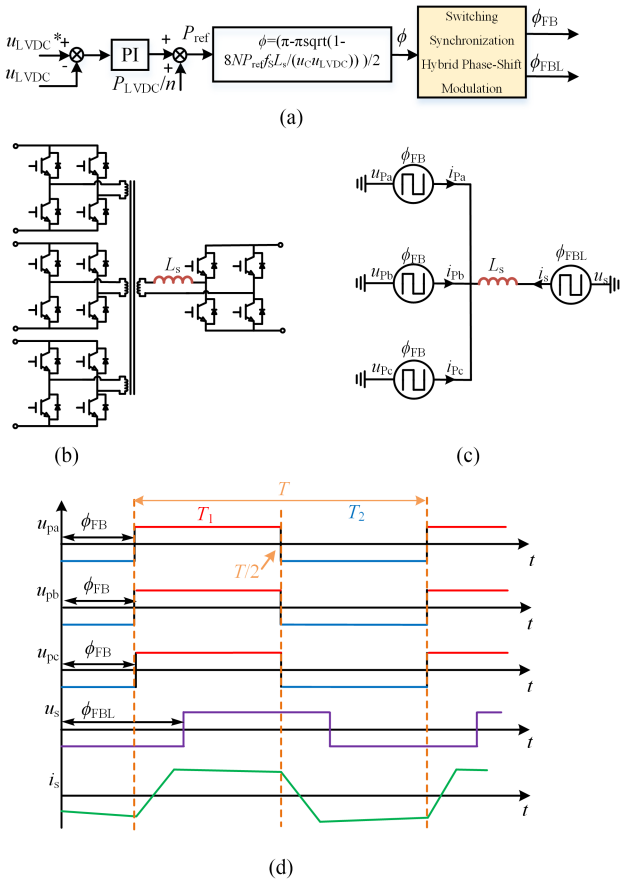

Fig. 5. Control and modulation strategy of SIQAB-stage. (a) SIQAB-stage control strategy. (b) SIQAB-stage circuit. (c) SIQAB-stage equivalent model. (d) SSHPSM modulation method.

transfer between the primary and secondary sides is controlled by phase-shift modulation.

With the proposed SSHPSM method, in a switching cycle of SIQAB-stage, there are two steady-state stages T_1 and T_2. During T_1 and T_2, the equivalent model of high frequency link (HFL) established by the three-phase SM capacitors of CHB-stage and primary side H-bridges of SIQAB-stage is shown in Fig. 6. It can be seen the three-phase SM capacitors are interconnected by the full bridges with their transformer primary windings of SIQAB-stage in each half duty cycle and form the switched-capacitor circuits, so the primary side of SIQAB-stage operates in switched-capacitor mode, as shown in Fig. 7, the three-phase SMs are equivalent connected in parallel and their voltages are same at the end of the half duty cycle, which is defined as voltage clamp. Based on the characteristics of switched-capacitor circuits, the transfer and cancellation process of low-frequency ripple will be analyzed in the following sections.

B. Transfer Analysis of Low-Frequency Ripple by SSHPSM With Circuit Model

In the switched-capacitor circuits equivalent model, as shown in Fig. 7, three-phase SM capacitors are equivalent connected in parallel in each high-frequency half duty cycle, the three-phase SM capacitor voltages are clamped each other and tend to

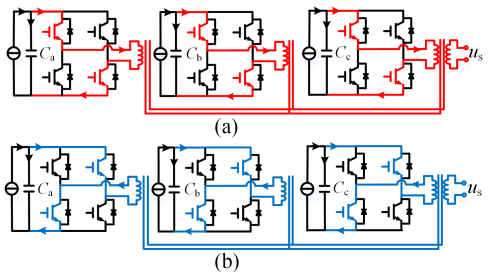

Fig. 6. Equivalent model of primary H-bridges of HFL. (a) T_1. (b) T_2.

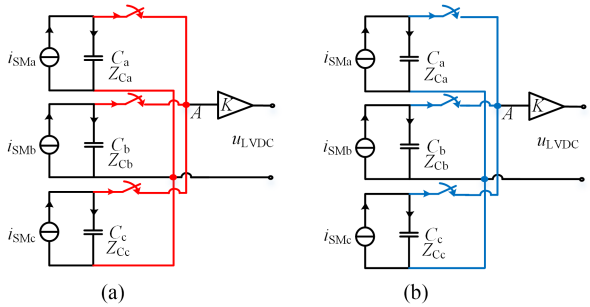

Fig. 7. Equivalent model of switched-capacitor circuits. (a) T_1. (b) T_2.

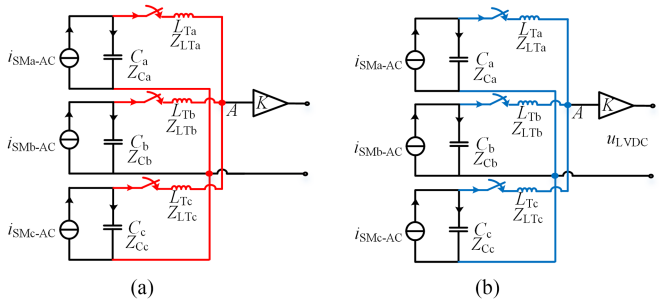

Fig. 8. Equivalent model of switched-capacitor circuits considering leakage inductance. (a) T_1. (b) T_2.

be consistent. The u_{LVdc} is the LVdc bus voltage, K is the SIQAB-stage voltage conversion gain. Neglecting the switching-frequency components of i_{SMx}, the CHB-stage can be equivalent to a current source, which is composed of a dc current source superimposed with an ac current source, and the SM charging current i_{SMx} consists of the dc component $i_{\mathrm{SMx\text{-}dc}}$ and ac component $i_{\mathrm{SMx\text{-}ac}}$. For the dc component $i_{\mathrm{SMx\text{-}dc}}$, the SM capacitance impedance tends to infinity, so the dc power is transferred to the LVdc bus according to the control strategy shown in Fig. 5(a). For the ac component $i_{\mathrm{SMx\text{-}ac}}$, the specific analysis of the ripple-current transmission process is as follows; in practical application, the transformer has leakage inductance, considering the influence of leakage impedance, the switched-capacitor circuits are shown in Fig. 8, where C_{x}, Z_{Cx} are the SM capacitance and the capacitance impedance of the CHB-stage, and $Z_{\mathrm{Cx}} = 1/j\omega C_{\mathrm{x}}$. L_{TTx} and Z_{LTTx} are the transformer leakage inductance and the inductance impedance of the SIQAB-stage primary side, and $Z_{\mathrm{LTTx}} = j\omega L_{\mathrm{TTx}}$. Defining set $\mathrm{P} = \{\mathrm{a}, \mathrm{b}, \mathrm{c}\}$ and $\mathrm{x}, \mathrm{y}, \mathrm{z} \in \mathrm{P}$, then the equivalent input impedance of the phase-x of SIQAB-stage is defined, as Z_{ex} shown in (6), at the bottom of this page, which includes the Z_{LTTx} of phase-x and Z_{Cy} and Z_{LTTy} of the other two phases. The ripple-current flowing into the SM capacitor and SIQAB-stage are defined as $i_{\mathrm{Cx\text{-}ac}}$ and $i_{\mathrm{Qx\text{-}ac}}$, respectively. According to the relationship between Z_{Cx} and Z_{ex}, $i_{\mathrm{Cx\text{-}ac}}$ and $i_{\mathrm{Qx\text{-}ac}}$ can be expressed as (7)

$$\begin{cases} i_{\mathrm{SMx-ac}} = i_{\mathrm{Cx-ac}} + i_{\mathrm{Qx-ac}} \\ i_{\mathrm{Cx-ac}} = i_{\mathrm{SMx-ac}} \cdot Z_{\mathrm{ex}} / \left(Z_{\mathrm{Cx}} + Z_{\mathrm{ex}}\right) \\ i_{\mathrm{Qx-ac}} = i_{\mathrm{SMx-ac}} \cdot Z_{\mathrm{Cx}} / \left(Z_{\mathrm{Cx}} + Z_{\mathrm{ex}}\right). \end{cases} \tag{7}$$

For Fig. 8, taking phase-x as an example, $i_{\mathrm{SMx\text{-}ac}}$ of the other two phases is set to be open circuits, $i_{\mathrm{Qx\text{-}acy}}$ is the currents flowing into other two phases from the equivalent ac current source $i_{\mathrm{Qx\text{-}ac}}$, which can be expressed as

$$\begin{cases} i_{\mathrm{Qx-ac}} = \sum_{\mathrm{y}\in\mathrm{P},\mathrm{y}\neq\mathrm{x}} i_{\mathrm{Qx-acy}} \\ i_{\mathrm{Qx-acy}} = \frac{i_{\mathrm{Qx-ac}} \cdot (Z_{\mathrm{LTz}} + Z_{\mathrm{Cz}})}{Z_{\mathrm{LTy}} + Z_{\mathrm{LTz}} + Z_{\mathrm{Cy}} + Z_{\mathrm{Cz}}}, \mathrm{z} \neq \mathrm{y} \neq \mathrm{x}. \end{cases} \tag{8}$$

Taking phase-a as an example, according to the superposition theorem, the response of i_{Ca} is equal to the algebraic sum of the response of $i_{\mathrm{Ca\text{-}ac}}$, $i_{\mathrm{Qb\text{-}aca}}$ and $i_{\mathrm{Qc\text{-}aca}}$ by considering the equivalent ac current sources of phase-a, b, and c, which can be expressed as

$$\begin{aligned} i_{\mathrm{Ca}} &= i_{\mathrm{Ca-ac}} + i_{\mathrm{Qb-aca}} + i_{\mathrm{Qc-aca}} \\ &= \frac{i_{\mathrm{SMa-ac}} Z_{\mathrm{ea}}}{Z_{\mathrm{Ca}} + Z_{\mathrm{ea}}} + \frac{i_{\mathrm{SMb-ac}} Z_{\mathrm{Cb}}}{Z_{\mathrm{Cb}} + Z_{\mathrm{eb}}} \cdot \frac{Z_{\mathrm{LTc}} + Z_{\mathrm{Cc}}}{Z_{\mathrm{LTa}} + Z_{\mathrm{LTc}} + Z_{\mathrm{Ca}} + Z_{\mathrm{Cc}}} \\ &\quad + \frac{i_{\mathrm{SMc-ac}} Z_{\mathrm{Cc}}}{Z_{\mathrm{Cc}} + Z_{\mathrm{ec}}} \cdot \frac{Z_{\mathrm{LTb}} + Z_{\mathrm{Cb}}}{Z_{\mathrm{LTa}} + Z_{\mathrm{LTb}} + Z_{\mathrm{Ca}} + Z_{\mathrm{Cb}}}. \end{aligned} \tag{9}$$

Assuming the parameters of the SM capacitance and leakage inductance of HFT are consistent, that are, $Z_{\mathrm{Ca}} = Z_{\mathrm{Cb}} = Z_{\mathrm{Cc}} = 1/j\omega C$, $Z_{\mathrm{LTa}} = Z_{\mathrm{LTb}} = Z_{\mathrm{LTc}} = j\omega L_{\mathrm{T}}$, then (9) can be rewritten as (10) combined with (4)

$$i_{\mathrm{Ca}} = i_{\mathrm{Ca-ac}} + i_{\mathrm{Qb-aca}} + i_{\mathrm{Qc-aca}} = i_{\mathrm{SMa-ac}} \frac{1}{1 + \frac{1}{\omega^2 L_{\mathrm{T}} C}}. \tag{10}$$

It can be seen from (10) that the ripple-current cannot completely decouple with the SM capacitors due to the leakage inductance, but the leakage inductance can be reduced in design to minimize the influence. Therefore, the leakage inductance of the HFT of SIQAB-stage is designed to be as small as possible so that the i_{Ca} approaches zero, which means that the ripple-current $i_{\mathrm{SMx\text{-}ac}}$ is completely decoupled with the SM capacitor and transferred to the primary side of HFT of SIQAB-stage based on the low impedance characteristics of equivalent connected

$$Z_{\mathrm{ex}} = \frac{Z_{\mathrm{LTx}} \sum_{\mathrm{y}\in\mathrm{P},\mathrm{y}\neq\mathrm{x}} \left(Z_{\mathrm{LTy}} + Z_{\mathrm{Cy}}\right) + \sum_{\mathrm{y,z}\in\mathrm{P},\mathrm{z}\neq\mathrm{y}\neq\mathrm{x}} \left(Z_{\mathrm{LTy}} Z_{\mathrm{Cz}}\right) + \prod_{\mathrm{y}\in\mathrm{P},\mathrm{y}\neq\mathrm{x}} Z_{\mathrm{LTy}} + \prod_{\mathrm{y}\in\mathrm{P},\mathrm{y}\neq\mathrm{x}} Z_{\mathrm{Cy}}}{\sum_{\mathrm{y}\in\mathrm{P},\mathrm{y}\neq\mathrm{x}} \left(Z_{\mathrm{LTy}} + Z_{\mathrm{Cy}}\right)} \tag{6}$$

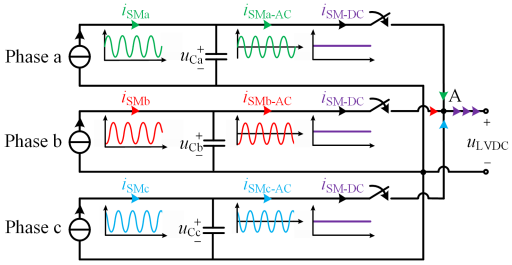

Fig. 9. Transfer process of ripple-current based on switched-capacitor circuits.

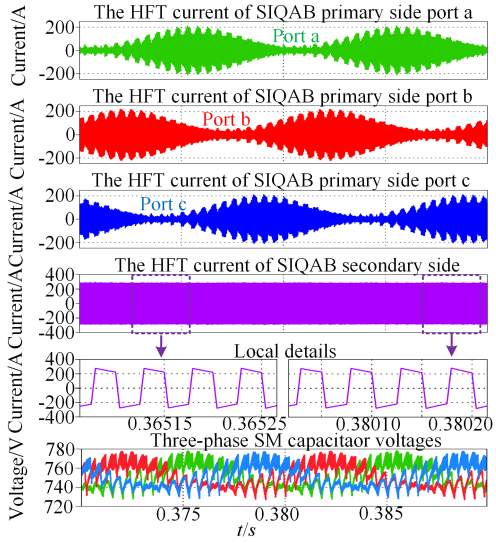

Fig. 10. SIQAB-stage HFT currents and three-phase SM capacitor voltages at the low-frequency ripple cycle.

in parallel without the additional ripple-power transfer control, and the primary side current of HFT is expressed as (11) based on double Fourier transformation and Taylor expansion, where, $i_{\text{p-dc}}$ is the dc component of HFT current i_{px}, which contains the magnetic current component, and $i_{\text{px-ac}}$ is the ripple component of HFT current, ω_{S} is high-frequency switching angular frequency of SIQAB-stage, it can be seen that the second-order-frequency component exists in the form of sideband harmonics with three-phase symmetry in the primary side current of HFT under high-frequency synchronization modulation

$$\begin{aligned} i_{\text{px}} &= i_{\text{p-dc}} + i_{\text{px-ac}} \\ &= \frac{2I_{\text{s}}g}{\pi}\sum_{m=1}^{\infty}\frac{\sin((2m-1)\omega_{\text{S}}t)}{2m-1} \\ &\quad + \frac{I_{\text{s}}g}{\pi}\sum_{m=1}^{\infty}\frac{\cos\left\{\left[(2m-1)\omega_{\text{S}} \pm 2\omega\right]t + \theta_{\text{x}}\right\}}{2m-1}. \end{aligned} \tag{11}$$

Therefore, the process of ripple transmission under high-frequency synchronization modulation can be equivalent as follows; Low frequency ac component $i_{\text{SM-ac}}$ is transferred to the point "A" in the switched-capacitor circuits based on the low impedance characteristic of the equivalent connected in parallel, and is canceled through magnetic coupling based on three-phase symmetry, which will be analyzed in the next section, only the dc current flows into the LVdc bus, as shown in Fig. 9. The HFT currents and SM capacitor voltage based on the switched-capacitor circuits is shown in Fig. 10, which verifies that the high-frequency synchronization modulation helps the transmission of low-frequency ripple, i.e., the second-order-frequency component exists in the form of high-frequency sideband harmonics with three-phase symmetry in the primary side current of HFT under high-frequency synchronization modulation, while the secondary side only contains the dc component, and the capacitor voltages of the three-phase SMs clamp each other and ripple in a small range, which can be approximated to be consistent due to the equivalently connected in parallel characteristics.

C. Suppression Analysis of Low-Frequency Ripple by SSHPSM With Magnetic Reluctance Model

In Section III-B, the process of low-frequency ripple transfer to the primary side of HFT under high-frequency synchronous modulation is analyzed. The process of ripple component cancellation through magnetic coupling is analyzed in detail in this section. The four winding transformer model is shown in Fig. 11(a). The primary side windings completely cover the core and the secondary side winding is divided into three parts, which are covered by the three ports winding of the primary side, respectively, to reduce the leakage inductance of the HFT, where W_{px}(x = a,b,c) is the three port winding of the primary side of SIQAB-stage, respectively, and W_{si}(i = 12,3) is the secondary side windings. The magnetic field strength and magnetic flux path is shown in Fig. 11(b) by ANSYS simulation of the transformer winding model, where Φ_{mi} is the magnetic flux covered by the primary winding, and R_{mi} is the magnetic reluctance corresponding to the $\Phi_{\text{m1,23}}$, Φ_{gi} is the magnetic flux flowing through the gap between the primary winding in the magnetic core, and R_{gi} is the magnetic reluctances corresponding to the Φ_{g}, F_{px} are the magnetomotive force of the primary side windings, respectively, which is equal to N_{px}*i_{px}, where $N_{\text{px(x = a,b,c)}}$ is the turns of primary winding, i_{px} is obtained in (11), F_{si} is the magnetomotive force of the secondary side windings. The leakage magnetic flux is mainly concentrated between the primary and secondary windings according to Fig. 11(b), so the leakage flux in the air is ignored and the equivalent leakage inductance obtained by simulation is about 2 uH, which conforms to the design of small leakage inductance, where $R_{\delta\text{i}1}$ and $R_{\delta\text{i}2}$ are the leakage magnetic reluctances corresponding to the leakage magnetic flux, respectively. The equivalent magnetic reluctances model is shown in Fig. 11(c), where $R_{\delta\text{i}}$ is $R_{\delta\text{i}1}$ and $R_{\delta\text{i}2}$ in parallel.

In Fig. 11(c), it is assumed that the transformer is symmetrical $N_{\text{px}} = N_{\text{p}}$, $R_{\text{mi}} = R_{\text{m}}$, $R_{\text{gi}} = R_{\text{g}}$, $R_{\delta\text{i}} = R_{\delta}$, $F_{\text{si}} = F_{\text{s}}$. According to the superposition theorem, the magnetic flux Φ_{m1} stimulated by the magnetomotive force of each winding can be expressed as (12), shown at the bottom of the next page. According to (12), the part containing ripple-current i_{px} in (11) will be canceled based on the three-phase symmetry, the magnetic flux in the

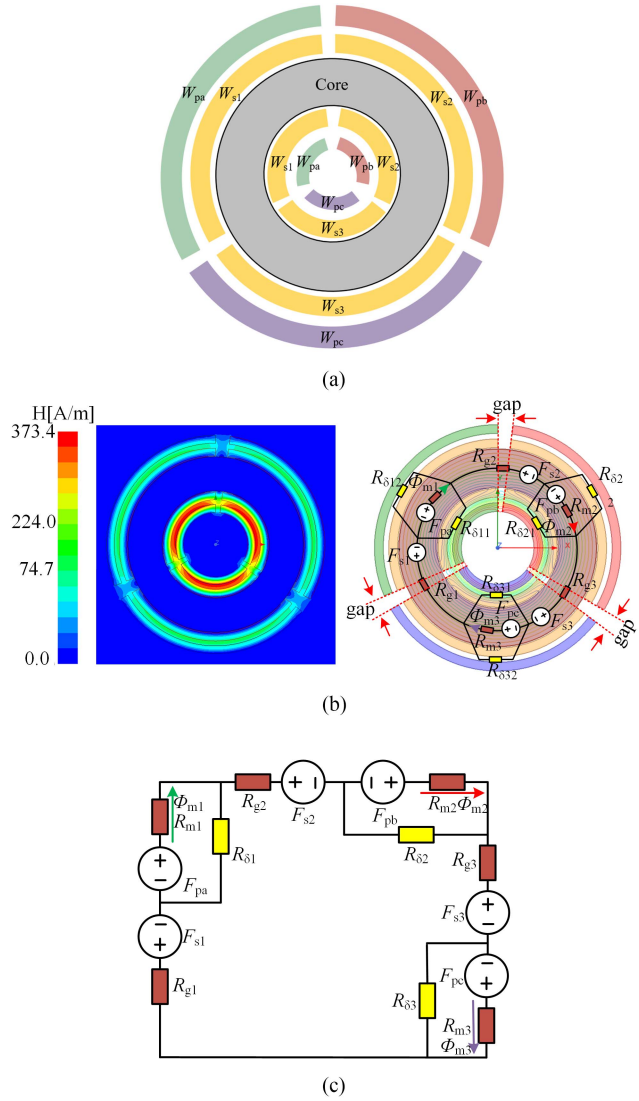

Fig. 11. Equivalent model of four winding transformer. (a) Transformer winding model. (b) Magnetic field strength and magnetic flux path of transformer winding model. (c) Magnetic reluctance model.

magnetic core can be further expressed as (13), shown at the bottom of this page, it can be seen that the magnetic flux in the magnetic core is composed of three parts 1) the part of the ripple component, which is not completely canceled due to the influence of leakage inductance; 2) the part stimulated by the dc component of primary side magnetomotive force F_{px}; 3) the part stimulated by the secondary side magnetomotive force F_{si}. The leakage inductance is on the "uH" order of magnitude and the magnetic inductance is on the "mH" order of magnitude. Therefore, R_δ is far greater than R_{m} and R_{g}. and the part 1 is far smaller than other two parts and can be ignored. The result of the common stimulated by the Part 2 and Part 3 is the magnetic flux generated by the magnetic current of the primary side.

It is approximately considered that in the magnetic reluctance model, based on the three-phase symmetry the magnetic flux in the magnetic core caused by low-frequency ripple-current is canceled in the main magnetic flux path and there is also slight leakage magnetic flux that is not completely canceled, which is consistent with the analysis of small leakage inductance design in Section III-B. The incompletely canceled magnetic flux will increase the magnetic flux density B according to (14), where S is the cross-sectional area of the core

$$B = \frac{\phi_{\mathrm{mi}}}{N \cdot S}. \tag{14}$$

The magnetic flux density under the traditional large capacitance scheme and the capacitance minimization scheme is shown in Fig. 12, in the traditional scheme, the ripple component is not transmitted to the HFT primary side to generate a magnetic flux, and its maximum magnetic flux intensity is 0.6132T. Under the proposed synchronization modulation, the ripple is transmitted to the HFT primary side, but the generated magnetic flux is canceled based on the three-phase symmetry, there is little leakage magnetic flux that is not completely canceled, and the maximum magnetic flux intensity is 0.6824T, a slight increase of 2.4%. It is verified that when the leakage inductance of the HFT is reduced as much as possible in the design, the ripple component with three-phase symmetry can decouple with the SM capacitor and transferred to the primary side of the HFT to cancel based on the

$$\Phi_{\mathrm{m1}} = \underbrace{\frac{N_{\mathrm{p}}\left(i_{\mathrm{p-dc}} + i_{\mathrm{pa-ac}}\right)}{\left[2\left(R_{\mathrm{m}}//R_\delta\right) + 3R_{\mathrm{g}}\right]//R_\delta + R_{\mathrm{m}}}}_{\text{Magnetic flux under } F_{\mathrm{pa}}} + \underbrace{\frac{N_{\mathrm{p}}\left(i_{\mathrm{p-dc}} + i_{\mathrm{pb-ac}}\right)}{\left[2\left(R_{\mathrm{m}}//R_\delta\right) + 3R_{\mathrm{g}}\right]//R_\delta + R_{\mathrm{m}}} \cdot \frac{R_\delta}{2\left(R_{\mathrm{m}}//R_\delta\right) + 3R_{\mathrm{g}} + R_\delta} \cdot \frac{R_\delta}{R_\delta + R_{\mathrm{m}}}}_{\text{Magnetic flux under } F_{\mathrm{pb}}}$$
$$+ \underbrace{\frac{N_{\mathrm{p}}\left(i_{\mathrm{p-dc}} + i_{\mathrm{pc-ac}}\right)}{\left[2\left(R_{\mathrm{m}}//R_\delta\right) + 3R_{\mathrm{g}}\right]//R_\delta + R_{\mathrm{m}}} \cdot \frac{R_\delta}{2\left(R_{\mathrm{m}}//R_\delta\right) + 3R_{\mathrm{g}} + R_\delta} \cdot \frac{R_\delta}{R_\delta + R_{\mathrm{m}}}}_{\text{Magnetic flux under } F_{\mathrm{pc}}} - \underbrace{F_{\mathrm{s}} \cdot \frac{3}{3\left(R_{\mathrm{m}}//R_\delta\right) + 3R_{\mathrm{g}}} \cdot \frac{R_\delta}{R_\delta + R_{\mathrm{m}}}}_{\text{Magnetic flux under } F_{\mathrm{s1,2,3}}} \tag{12}$$

$$\Phi_{\mathrm{m}} = \underbrace{\frac{N_{\mathrm{p}} i_{\mathrm{px-ac}}}{R_{\mathrm{m}} + R_\delta}}_{\text{Part 1: Not completely cancelled}} + \underbrace{\left[\underbrace{\frac{N_{\mathrm{p}} i_{\mathrm{p-dc}}\left(R_{\mathrm{g}} + R_\delta\right)}{R_{\mathrm{g}}R_{\mathrm{m}} + R_{\mathrm{g}}R_\delta + R_{\mathrm{m}}R_\delta}}_{\text{Part 2: Magnetic flux under dc component of } F_{\mathrm{pa,b,c}}} - \underbrace{\frac{F_{\mathrm{s}}R_\delta}{R_{\mathrm{m}}R_\delta + R_{\mathrm{g}}R_\delta + R_{\mathrm{m}}R_\delta}}_{\text{Part 3: Magnetic flux under } F_{\mathrm{s1,2,3}}}\right]}_{\text{Magnetic flux of the primary sidemagnetic current}}. \tag{13}$$

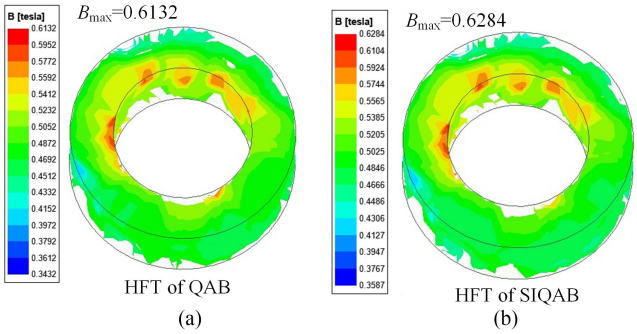

Fig. 12. Magnetic flux density in the ANSIS simulation. (a) Traditional large capacitance scheme. (b) Capacitance minimization scheme.

TABLE II
OPERATING PARAMETERS AND DEVICE SPECIFICATIONS

	Traditional large capacitance scheme	Capacitance minimization scheme
Port voltage /u_{px}, u_s	750V	
Switching frequency /$f_{Q,S}$	20kHz	
HFT RMS current at full load /$I_{rms\text{-}p}$, $I_{rms\text{-}s}$	80A, 240A	100A, 240A
Primary side switch /SiC	FF6MR12KM1[20]	FF3MR12KM1[21]
T_{on} of primary side switch /t_{on}=(t_{don}+t_r)	98ns	290ns
T_{off} of primary side switch /t_{off}=(t_{doff}+t_f)	170ns	106ns
Conduction resistance of primary side switch /R_{DS}	7.5mΩ	3.9mΩ
Secondary side switch /SiC	FF2MR12KM1[22]	
T_{on} of secondary side switch /t_{on}=(t_{don}+t_r)	141ns	
T_{off} of secondary side switch /t_{off}=(t_{doff}+t_f)	75ns	
Conduction resistance of primary side switch /R_{DS}	2.9mΩ	
Magnetic core material	nanocrystalline	
Magnetic core specification	(PC0074 ONL-130*80*50)*4	(PC0074 ONL-130*80*50)*5

magnetic coupling under the switched-capacitor circuits formed by synchronization modulation.

D. Power Losses Distribution and Efficiency of DC–DC-Stage Under Two Schemes

This section analyzes the power loss of the QAB-stage under the traditional large capacitance scheme and the SLQAB-stage under the proposed capacitance minimization scheme. In the traditional scheme, ripple-power is absorbed by the large capacitor, the primary and secondary side switches of QAB-stage only contain dc current component. Under the proposed scheme, ripple-power is transmitted to the SIQAB-stage, the primary side switch current of SIQAB-stage is the superposition of dc component and second-order-frequency ripple component. Combined with the operating conditions in Table IV, the SiC MOSFET can effectively improve the efficiency of the system at the switching frequency of 20 kHz due to the lower time intervals during switching ON and OFF, as well as smaller conduction resistance. The specifications of switches and cores in dc–dc-stage for power loss calculation is shown in Table II.

TABLE III
SINGLE SM CAPACITOR PARAMETERS AND SPECIFICATIONS

	Traditional large capacitance scheme	Capacitance minimization scheme
Capacitance constraints	$C \geq \frac{I_s g}{4\pi f_F \varepsilon u_C}$	$C \geq \frac{I_s g^2}{2 f_{SM} \varepsilon u_C}$
SM capacitance	6mF	0.73mF
Capacitor specification	(2.4mF/1200V) B25690C1248K203	(1mF/1200V) B25690A1108K203
Composition	3 in parallel	single
Volume	5.46dm^3*3=16.38dm^3	2.49 dm^3
Cost	$299.8*3=$899.4	$129.87

The switching power loss under the two schemes is shown in

$$\begin{cases} P_{swT} = \frac{1}{2} V_{sw} I_{swT} \left(t_{on} + t_{off}\right) f_Q \\ P_{swP} = \frac{1}{T_{2F}} \int_0^{T_{2F}} \frac{1}{2} V_{sw} I_{swP} \left(t_{on} + t_{off}\right) f_S dt \end{cases} \tag{15}$$

where "T" and "P" represent the traditional and proposed scheme, respectively, $P_{swT,P}$ are the switching losses, V_{sw} and $I_{swT,P}$ are the voltage and current at the switching time, respectively, and t_{ON} and t_{OFF} are the time intervals during switching ON and OFF, respectively, f_Q and f_s are the switching frequency of the QAB-stage and SLQAB-stage, respectively. The conduction losses of the dc–dc-stage switches can be expressed as

$$\begin{cases} P_{conT} = I_{rmsT}^2 R_{DS} \\ P_{conP} = I_{rmsP}^2 R_{DS} \end{cases} \tag{16}$$

where $P_{conT,P}$ are the conduction loss, $I_{rmsT,P}$ are rms currents, R_{DS} are the conduction resistance

The power losses of HFT are mainly distributed on the magnetic core and winding, which can be calculated by the existing research [23], and expressed as

$$\begin{cases} P_{core} = f_{Q,S} \int_0^{\frac{1}{f_{Q,S}}} \left(\frac{K \left| \frac{dB(t)}{dt} \right|^{\alpha} |B(t)|^{\beta-\alpha}}{(2\pi)^{\alpha-1} \int_0^{2\pi} |\cos\theta|^{\alpha} 2^{\beta-\alpha} d\theta} \right) dt \\ P_{wind} = \sum_{i=1}^{h} I_{rms}(h)^2 R_{ac}(h) \end{cases} \tag{17}$$

where P_{core} and P_{wind} are the magnetic core loss and winding loss, B is the magnetic flux density, K, α, and β are determined by the magnetic core characteristics, h is the FFT component index, $R_{ac}(h)$ is the winding resistance at the h_{th} frequency range, $I_{rms}(h)$ is the rms current component at the h_{th} frequency range.

The comparison of power losses distribution and efficiency between the two schemes under different load conditions is shown in Fig. 13. Under the proposed capacitance minimization scheme, the efficiency of SIQAB-stage can reach to 96% and still operate with high efficiency.

E. Capacitance Constraint Analysis Under SSHPSM Method

After the second-order-frequency ripple is suppressed, the SM capacitor only needs to absorb the switching harmonic generated by the SM H-bridge and the SIQAB-stage H-bridge during the pulsewidth modulation process. Since the switching frequency of the SIQAB-stage is much higher than that of the CHB-stage, the harmonic current handled by the SM capacitor mainly comes from the SM H-bridge. In a switching cycle, the charging energy

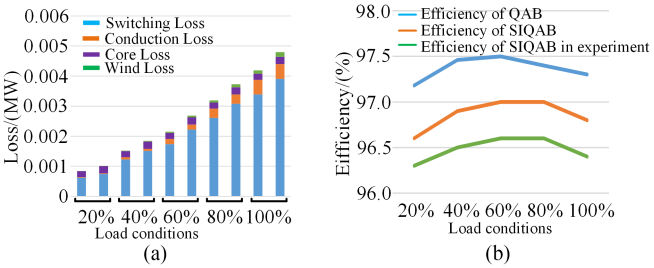

Fig. 13. Power losses distribution and efficiency of DC–DC-stage under two schemes. (a) Power losses distribution. (b) Efficiency of DC–DC-stage.

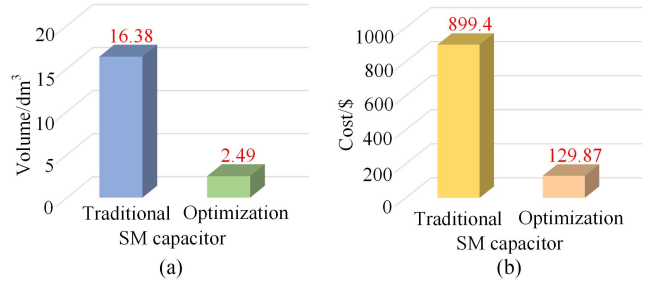

Fig. 14. Histogram of the SM capacitor volume and cost comparison. (a) Volume comparison. (b) Cost comparison.

of SM capacitor is

$$\Delta E_{\mathrm{SM}} = \frac{i_{\mathrm{SMx\,max}} D_{\mathrm{SM}}}{f_{\mathrm{SM}}} \tag{18}$$

where the i_{SMxmax} is the maximum average value of the SM charging current shown in (3), D_{SM} is the duty cycle of the SM H-bridge switch, and the maximum value is equal to the voltage modulation ratio g which is not more than 1, f_{SM} is the switching frequency of CHB-stage. And the capacitor voltage ripple caused by ΔE_{SM} is

$$\varepsilon u_{\mathrm{c}} = \frac{\Delta E_{\mathrm{SM}}}{C_{\mathrm{x}}} = \frac{I_{\mathrm{s}} g^2}{2 C_{\mathrm{x}} f_{\mathrm{SM}}}. \tag{19}$$

By combining (18) and (19), the constraint of the optimized SM capacitance is

$$C \geq \frac{I_{\mathrm{s}} g^2}{2 f_{\mathrm{SM}} \varepsilon u_{\mathrm{C}}}. \tag{20}$$

The capacitance constraint comparison with the traditional large capacitance scheme and selected the capacitor specifications, as shown in Table III, according to the operating conditions of Table IV. Compared with the traditional large capacitor scheme, the optimized capacitor volume is reduced by 85%, and the cost is reduced by 85.6%, as shown in Fig. 14.

IV. Influence of the Practical Nonideal Conditions on Switched-Capacitor Circuits

In theory, SIQAB-stage primary side gate signals of the three phase SM share the same signal and they should be strict consistency in phase and we define it as switch synchronization. In practical application, there are some nonideal factors, including

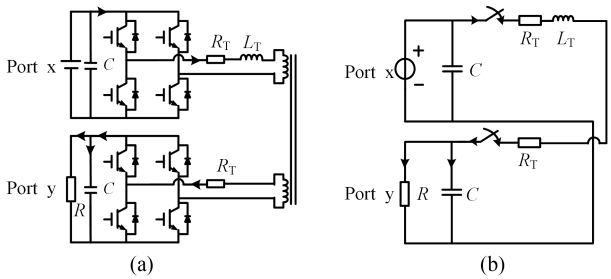

Fig. 15. SIQAB-stage primary side ports model. (a) Simulation model. (b) Equivalent circuit model.

1) the tiny difference of the switch signal due to circuit parameters, which is defined as "nonideal switch synchronization signal," 2) the inconsistency of primary side leakage inductance of HFT caused by manufacturing processes, which is defined as "the primary side leakage inductance inconsistency in HFT". The effectiveness of the switched-capacitor circuits under nonideal factors is analyzed in this section.

A. Influence of the Nonideal Switch Synchronization Signal

From Fig. 5(b), SIQAB-stage have only one inductor on the secondary side, while only leakage inductance exists on the three-phase primary side bridges. This section will discuss the sensitivity of circulating power between the primary side H-bridges to the nonideal switch synchronization signal, arising from mismatch between the rise and fall times of the switches across different primary side H-bridges and to the winding resistance variation of the various primary side windings. For the arbitrary two ports of SIQAB-stage primary side H-bridges, as shown in Fig. 15(a) and the equivalent circuit model is shown in Fig 15(b), one port is connected to a voltage source u_{i} and the other is connect to a 50 Ω load, the winding resistance R_{T} sets to 0.1 Ω, the unequal phase-shift ϕ_{xy} is only caused by hardware factors as the primary operation in synchronous mode. And considering the practical possibilities the upper limits is set 0.05° to simulate the incomplete synchronization of SIQAB primary side full bridge switch signal. First, we analyze the effect of leakage inductance as the inductance L_{T} is changed from 217 uH to 1 uH.

If the converter in Fig. 15 operates in DAB mode when a practical phase shift exists, the transmission power satisfies (1), and the output voltage u_{o} of port y can be further expressed as

$$u_{\mathrm{o}} = \frac{N u_{\mathrm{i}} R}{2\pi f_{\mathrm{S}} L_{\mathrm{T}}} \phi_{\mathrm{xy}} \left(1 - \frac{\phi_{\mathrm{xy}}}{\pi}\right). \tag{21}$$

If the converter in Fig. 15 operates in switched-capacitor mode, the u_{o} should same with the input voltage.

For the simulation, as shown in Fig. 16, the unequal phase-shift ϕ_{xy} caused by hardware factors is 0.05°; the inductance changes from 217 uH to 1 uH. When inductance is 217 uH, the simulation output voltage equals to result of (21) and the converter operation in DAB mode; as inductance decrease, the simulation results gradually deviate from the calculated results by (21). When the inductance is 1 uH, the output voltage is as

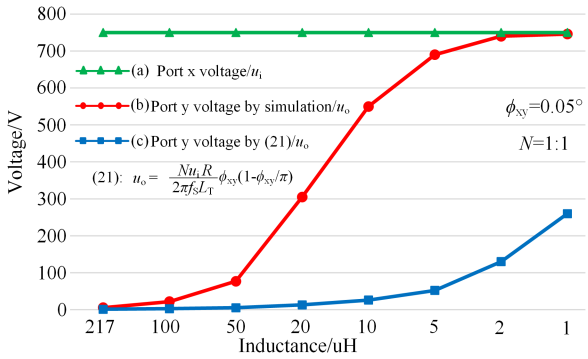

Fig. 16. Variation curve of ports voltage with inductance.

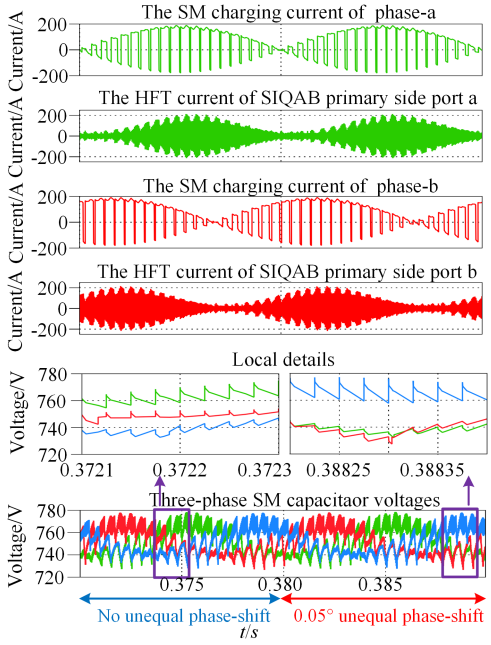

Fig. 17. SM charging current of phase-a and -b and HFT currents of primary sides at the low-frequency ripple cycle.

same as input voltage and the converter operates in switched-capacitor mode. Therefore, when the leakage inductance of HFT is reduced as much as possible in the design under the proposed scheme, the primary side H-bridges of SIQAB operate in switched-capacitor mode under synchronization modulation.

Based on synchronous modulation and the SM capacitor voltage clamp of switched-capacitor circuits, when the leakage inductance design is as small as 2 uH and the leakage inductance inconsistency is slightly less than 0.1 uH, the SM charging currents, HFT primary side currents and three-phase SM capacitor voltages are shown in Fig. 17. The phase-shift angle of 0.05° between port x and port y is set to mimic the phase difference of the switch synchronization signal caused by hardware factors, the SM charging currents and HFT currents ripple at low-frequency, which is equivalent to the load change of SIQAB-stage primary side port, the SM charging current and HFT current of each port are consistent, and the amplitude of SM charging current is consistent with that of HFT current. Therefore, there is no large switched-capacitor current, reactive current and circulating power between SIQAB-stage primary side ports due to the voltage clamping characteristics of switched-capacitor circuits. The nonideal switch synchronization signal has almost no effect on the transfer and cancellation of ripple-current based on the switched-capacitor characteristics.

In addition, as the charging current i_{SMa}, i_{SMb}, i_{SMc} at the input is controlled by ac side current loop, they are three phase symmetrical and transferred to the transformer primary side of SIQAB according to the impedance analysis in Section III-B. Under the abovementioned unbalanced conditions, there is no significant difference in the charging current between ports and the SM capacitor voltage caused by hardware factors ripple in a small range due to the SM capacitor voltage clamp of the switched-capacitor circuits, as shown in Fig. 17, the capacitor voltage difference between arbitrary two ports of SIQAB primary side H-bridges is less than 40 V, and the ripple is less than 5.3%, with variations in a small range in either SM capacitor voltage or in leakage inductance, the unequal power flow through each phase at the input is in a small range.

B. Influence of the Primary Side Leakage Inductance Inconsistency in HFT

In the previous section, it was analyzed that the leakage inductance of HFT was designed to be very small in the switched-capacitor circuits. The influence of the inconsistency of the primary leakage inductance of HFT on the switched-capacitor circuits will be further analyzed. Generally, we assuming the parameters of the SM capacitance are consistent, i.e., $Z_{\mathrm{Ca}} = Z_{\mathrm{Cb}} = Z_{\mathrm{Cc}} = 1/j\omega C_{\mathrm{a}}$. But due to the difference in manufacturing process of multiwinding transformers, the leakage inductance of each primary side winding is inconsistent. Supposing that ΔL_{T1} is the difference value between L_{Ta} and L_{Tb}, and ΔL_{T2} is the difference between L_{Ta} and L_{Tc}, then the leakage inductance impedance of the transformer primary side can be rewritten as $Z_{\mathrm{LTa}} = j\omega L_{\mathrm{Ta}}$, $Z_{\mathrm{LTb}} = j\omega(L_{\mathrm{Ta}}+\Delta L_{\mathrm{T1}})$, $Z_{\mathrm{LTc}} = j\omega(L_{\mathrm{Ta}}+\Delta L_{\mathrm{T2}})$, $i_{\mathrm{Ca\text{-}ac}}$, and $i_{\mathrm{Qa\text{-}ac}}$ in (7) can be further expressed as (22) shown at the bottom of this page, and the ripple-current $i_{\mathrm{Qb\text{-}aca}}$ and $i_{\mathrm{Qc\text{-}aca}}$ can be written as

$$\begin{cases} i_{\mathrm{Qb-aca}} = i_{\mathrm{Qb-ac}} \cdot \frac{\omega^2 C_{\mathrm{a}}(L_{\mathrm{Ta}}+\Delta L_{\mathrm{T2}})+1}{\omega^2 C_{\mathrm{a}}(2L_{\mathrm{Ta}}+\Delta L_{\mathrm{T2}})+2} \\ i_{\mathrm{Qc-aca}} = i_{\mathrm{Qc-ac}} \cdot \frac{\omega^2 C_{\mathrm{a}}(L_{\mathrm{Ta}}+\Delta L_{\mathrm{T1}})+1}{\omega^2 C_{\mathrm{a}}(2L_{\mathrm{Ta}}+\Delta L_{\mathrm{T1}})+2} \end{cases} \tag{23}$$

where due to the frequency of the ripple-current studied in this article is mainly second-order-frequency, the ω of (22) and (23)

$$\begin{cases} i_{\mathrm{Ca-ac}} = i_{\mathrm{SMa-ac}} \left(\frac{\omega^4 C_{\mathrm{a}}^2 \left(3L_{\mathrm{Ta}}^2 + 2L_{\mathrm{Ta}}\Delta L_{\mathrm{T1}} + 2L_{\mathrm{Ta}}\Delta L_{\mathrm{T2}} + \Delta L_{\mathrm{T1}}\Delta L_{\mathrm{T2}}\right) + \omega^2 C_{\mathrm{a}}(4L_{\mathrm{Ta}} + \Delta L_{\mathrm{T1}} + \Delta L_{\mathrm{T2}}) + 1}{\omega^4 C_{\mathrm{a}}^2 \left(3L_{\mathrm{Ta}}^2 + 2L_{\mathrm{Ta}}\Delta L_{\mathrm{T1}} + 2L_{\mathrm{Ta}}\Delta L_{\mathrm{T2}} + \Delta L_{\mathrm{T1}}\Delta L_{\mathrm{T2}}\right) + 2\omega^2 C_{\mathrm{a}}(3L_{\mathrm{Ta}} + \Delta L_{\mathrm{T1}} + \Delta L_{\mathrm{T2}}) + 3} \right) \\ i_{\mathrm{Qa-ac}} = i_{\mathrm{SMa-ac}} \left(\frac{\omega^2 C_{\mathrm{a}}(2L_{\mathrm{pa}} + \Delta L_{\mathrm{p1}} + \Delta L_{\mathrm{p2}}) + 2}{\omega^4 C_{\mathrm{a}}^2 \left(3L_{\mathrm{Ta}}^2 + 2L_{\mathrm{Ta}}\Delta L_{\mathrm{T1}} + 2L_{\mathrm{Ta}}\Delta L_{\mathrm{T2}} + \Delta L_{\mathrm{T1}}\Delta L_{\mathrm{T2}}\right) + 2\omega^2 C_{\mathrm{a}}(3L_{\mathrm{Ta}} + \Delta L_{\mathrm{T1}} + \Delta L_{\mathrm{T2}}) + 3} \right) \end{cases} \tag{22}$$

TABLE IV
SIMULATION PARAMETERS OF TWO SCHEMES

	Mode1	Mode2
CHB-stage parameters		
SM capacitor voltage/u_C	750V	750V
RMS value of line to line voltage/u_x	6kV	6kV
Rated active power/P	1.2MW	1.2MW
AC fundamental frequency/f_F	50Hz	50Hz
PWM carrier frequency/f_{SM}	2kHz	2kHz
SM capacitance/C	6mF	0.73mF
Number of SM of phase-x/n	8	8
DC/DC-stage parameters		
Transformer turns ratio/N	1:1:1:1	1:1:1:1
LVDC bus voltage/u_{LVDC}	750V	750V
Filtering inductance/L_F	3mH	3mH
The sum of the external inductance and the equivalent leakage inductance/L_{eq}	39uH	13uH
Switching frequency/f_Q, f_S	20kHz	20kHz

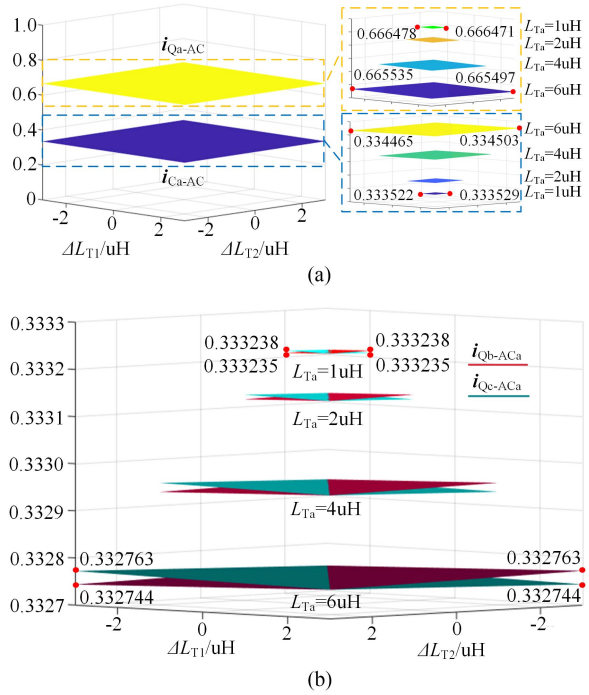

Fig. 18. Second-order-frequency ripple-current distribution of phase-a with the change of leakage inductance. (a) $i_{Ca\text{-}ac}$ to SM capacitor and $i_{Qa\text{-}ac}$ to the SIQAB-stage. (b) $i_{Qb\text{-}aca}$ and $i_{Qc\text{-}aca}$ from phase-b and phase-c to phase-a.

is equal to 200π. According to the small leakage design in Section III-C and manufacturing technique of the transformer in practical application [24], the range of L_{Ta} is set as 1–6 uH, ΔL_{T1} and ΔL_{T2} are set to $\pm 5\%$ of the L_{Ta}, and C_a is set based on the operation conditions in Table IV. Based on the second-order-frequency ripple-current analyzed in (22) and (23), the ripple-current distribution can be plotted in Fig. 18(a) and (b). It can be seen from Fig. 18 that, the variation of the ripple-current transmission caused by the leakage inductance difference ΔL_{T1} and ΔL_{T2} between the primary side three ports of the four-port

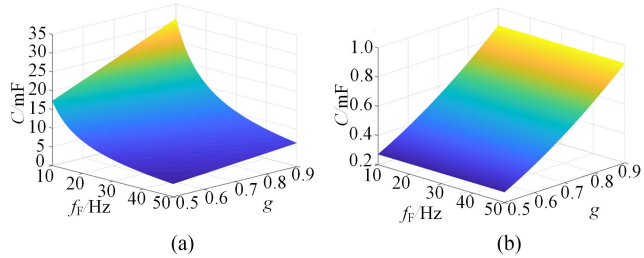

Fig. 19. Comparison of SM capacitance under two schemes. (a) Traditional scheme. (b) Capacitance minimization scheme.

transformer is within 0.004%, which can be considered as no effect. With the increase of the leakage inductance of the three ports, $i_{Ca\text{-}ac}$ and $i_{Qa\text{-}ac}$ change from 33.352%, 66.550% to 33.45%, 66.648% and the difference is only 0.01% and 0.01%; $i_{Qb\text{-}aca}$ and $i_{Qc\text{-}aca}$ change from 33.324%, 33.324% to 33.274%, 33.274%, respectively, and the difference is only 0.05% and 0.05%. The above variations indicate that the order of magnitude of HFT leakage inductance is very small under the small leakage inductance design, the primary side leakage inductance inconsistency has little influence on the ripple-current transfer and cancellation based on the switched-capacitor characteristic.

V. OPERATION FEASIBILITY EVALUATION FOR TYPICAL CRITICAL CONDITIONS

The topology shown in Fig. 2 can be used for motor drive and grid-tied control. The operation feasibility of the proposed scheme should be evaluated in the case of the typical critical conditions. When the system operates in low-frequency operation of motor drive conditions, the large capacitor is needed to suppress the low-frequency ripple for traditional CHB; when the system operates in three-phase voltage asymmetry for grid-tied conditions, additional zero-sequence component will be generated, and the large capacitor is also needed to suppress the low-frequency ripple for traditional CHB. In this section, the suppression effect of low-frequency ripple in the low-frequency operation for motor drive conditions and the fault ride through ability of three-phase voltage asymmetry for grid-tied conditions are further evaluated.

A. Low-Frequency Operation for Motor Drive Conditions

The CHB-SIQAB based on the proposed capacitance minimization scheme can also be used in the field of motor drive. When the frequency of motor variable frequency *V/F* control rises from 0 Hz to rated frequency, the converter will experience low-frequency operation [25]. According to the capacitance constraint shown in (5), the lower the output frequency is, the larger capacitor is required to suppress the second-order-frequency voltage ripple [26]. According to the parameters in Table IV and the capacitance constraint in (5), the variation curve of the SM capacitance with the frequency f_F and the modulation ratio g is shown in Fig 19(a), where the variation range of f_F is 10—50 Hz, the variation range of g is 0.5–0.9, and the ripple coefficient ε is 0.05. It can be seen that the

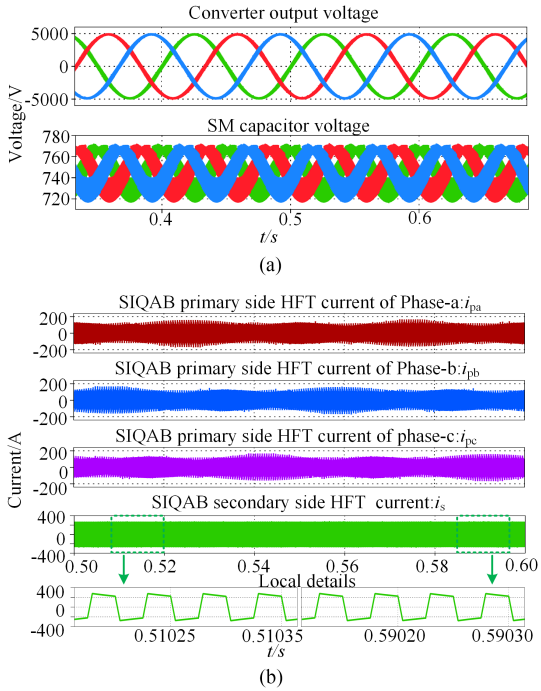

Fig. 20. Verification waveforms of the ripple component cancellation under low-frequency operation at 10 Hz. (a) Waveforms of output voltage and SM capacitor voltage. (b) Waveforms of HFT current of SIQAB-stage.

SM capacitance is significantly influenced by the operating frequency, and the lower the frequency is, the greater capacitance is required.

According to the principle of the ripple-current decoupling with the SM capacitor and the analysis of ripple-current cancellation at the primary side of the SIQAB-stage based on the three-phase symmetry, the proposed SSHPSM method is not affected by the frequency of the ripple component. Therefore, the capacitance constraint still only needs to consider the switching frequency of SM shown in (20). As shown in Fig 19(b), the capacitance of the CHB-SIQAB remains unchanged when it operates in the low-frequency operation. When CHB-SIQAB operates for motor driver, the simulation test waveforms of CHB-SIQAB operating in low-frequency operation with proposed SSHPSM method are shown in Fig. 20. Fig. 20(a) is the capacitor voltage waveform of SM when the operating frequency is 10 Hz, and the ripple is only 5%. In Fig. 20(b) the second-order-frequency ripple-current still can be canceled in the primary side of SIQAB-stage, so the secondary side current i_s only contains the dc component, which proves that the proposed capacitance minimization achieved by SSHPSM method and the capacitance constraint will not be affected under low-frequency operation.

B. Three-Phase Voltage Asymmetry Fault Ride-through for Grid-tied Conditions

Three-phase voltage asymmetry is a typical condition of low-voltage distribution network. For the medium and high voltage bus connected by CHB-SIQAB, voltage asymmetry is not allowed in the power supply specification. However, under fault conditions, such as short circuit to ground, three-phase voltage asymmetry will occur. If the fault cannot be eliminated within a certain time, the protection system will disconnect the fault line. When the three-phase voltage asymmetry occur under the fault condition in the MVac grid, the additional zero-sequence component will be generated. According to the symmetrical component theory, the voltage and current expression of the grid side under the three-phase voltage asymmetry condition can be obtained as

$$\begin{cases} u_{\mathrm{x}} = U_{\mathrm{s}}^{+}\sin\left(\omega t+\theta_{\mathrm{x}}^{+}\right)+U_{\mathrm{s}}^{-}\sin\left(\omega t+\theta_{\mathrm{x}}^{-}\right) \\ i_{\mathrm{x}} = I_{\mathrm{s}}^{+}\sin\left(\omega t+\varphi_{\mathrm{x}}^{+}\right)+I_{\mathrm{s}}^{-}\sin\left(\omega t+\varphi_{\mathrm{x}}^{-}\right) \end{cases} \tag{24}$$

where $U_s{}^+$ and $U_s{}^-$ are the positive and negative-sequential components of the voltage amplitude of the grid, $\theta_x{}^+$ and $\theta_x{}^-$ are the initial phase angles of the three-phase positive- and negative-sequence voltage components, $I_s{}^+$ and $I_s{}^-$ are the positive- and negative-sequential components of the current amplitude of the grid, $\varphi_x{}^+$ and $\varphi_x{}^-$ are the initial phase angles of the three-phase positive- and negative-sequence current components. The switching function expression of SM under the condition of three-phase asymmetry is derived as (25), where g^+ and g^- are the three-phase positive- and negative-sequence modulation ratios, and the maximum value is 1

$$s_{\mathrm{i}} = g^{+}\sin\left(\omega t+\theta_{\mathrm{x}}^{+}\right)+g^{-}\sin\left(\omega t+\theta_{\mathrm{x}}^{-}\right). \tag{25}$$

Taking phase-a as an example, combining (24) and (25), the charging current of the SM capacitor under the three-phase asymmetric condition can be expressed as (26) which contains the dc component, as well as positive-, negative-, and zero-sequence components

$$\begin{aligned} i_{\mathrm{SMx}}(t) &= s_i(t)\cdot i_{\mathrm{x}}(t) \\ &= \underbrace{I_{\mathrm{s}}^{+}g^{+}\frac{\cos(\theta_{\mathrm{x}}^{+}-\varphi_{\mathrm{x}}^{+})}{2}+I_{\mathrm{s}}^{-}g^{-}\frac{\cos(\theta_{\mathrm{x}}^{-}-\varphi_{\mathrm{x}}^{-})}{2}}_{\text{dc component}} \\ &= \underbrace{I_{\mathrm{s}}^{-}g^{+}\frac{\cos(\theta_{\mathrm{x}}^{+}-\varphi_{\mathrm{x}}^{-})}{2}+I_{\mathrm{s}}^{+}g^{-}\frac{\cos(\theta_{\mathrm{x}}^{-}-\varphi_{\mathrm{x}}^{+})}{2}}_{\text{dc component}} \\ &+\underbrace{I_{\mathrm{s}}^{+}g^{+}\frac{-\cos(2\omega t+\theta_{\mathrm{x}}^{+}+\varphi_{\mathrm{x}}^{+})}{2}}_{\text{positive sequence component}}+\underbrace{I_{\mathrm{s}}^{-}g^{-}\frac{\cos(2\omega t+\theta_{\mathrm{x}}^{-}-\varphi_{\mathrm{x}}^{+})}{2}}_{\text{negative sequence component}} \\ &+\underbrace{I_{\mathrm{s}}^{+}g^{+}\frac{-\cos(2\omega t+\theta_{\mathrm{x}}^{-}+\varphi_{\mathrm{x}}^{+})}{2}+I_{\mathrm{s}}^{-}g^{-}\frac{-\cos(2\omega t+\theta_{\mathrm{x}}^{+}+\varphi_{\mathrm{x}}^{-})}{2}}_{\text{zero sequence component}}. \end{aligned} \tag{26}$$

When the three-phase voltage asymmetry occurs, the $i_{\mathrm{SMx\text{-}ac}}$ will still flow into HFL, where the positive- and negative-sequence components can still decouple with the capacitor and be canceled based on the three-phase symmetry, but the zero-sequence component cannot be canceled due to the same amplitude and phase. Combining (4) and (26), $i_{\mathrm{SMx\text{-}ac}}$ is shown

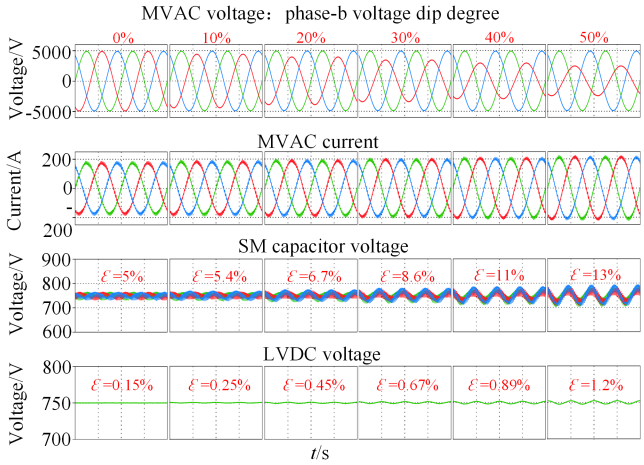

Fig. 21. Fault ride through ability of three-phase voltage asymmetry for grid-tied operation.

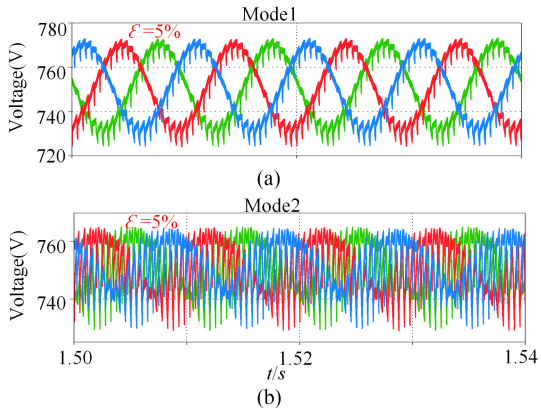

Fig. 22. Waveforms of three-phase SM capacitor voltage. (a) Mode 1. (b) Mode 2.

in (27). Combining (27) and (10) i_{Ca} can be expressed as (28)

$$\begin{cases} i_{\mathrm{SMa\_ac}} \\ = \frac{-I_s^+ g^+ \cos(2\omega t+\theta_x^+ +\varphi_x^+)}{2} + \frac{-I_s^- g^- \cos(2\omega t+\theta_x^- +\varphi_x^-)}{2} \\ + \frac{-I_s^- g^+ \cos(2\omega t+\theta_x^+ +\varphi_x^-)}{2} + \frac{-I_s^+ g^- \cos(2\omega t+\theta_x^- +\varphi_x^+)}{2} \\ i_{\mathrm{SMb\_ac}} \\ = \frac{-I_s^+ g^+ \cos(2\omega t+\theta_x^+ +\varphi_x^+ -2\pi/3)}{2} + \frac{-I_s^- g^- \cos(2\omega t+\theta_x^- +\varphi_x^+ +2\pi/3)}{2} \\ + \frac{-I_s^- g^+ \cos(2\omega t+\theta_x^+ +\varphi_x^-)}{2} + \frac{-I_s^+ g^- \cos(2\omega t+\theta_x^- +\varphi_x^+)}{2} \\ i_{\mathrm{SMc\_ac}} \\ = \frac{-I_s^+ g^+ \cos(2\omega t+\theta_x^+ +\varphi_x^+ +2\pi/3)}{2} + \frac{-I_s^- g^- \cos(2\omega t+\theta_x^- +\varphi_x^- -2\pi/3)}{2} \\ + \frac{-I_s^- g^+ \cos(2\omega t+\theta_x^+ +\varphi_x^-)}{2} + \frac{-I_s^+ g^- \cos(2\omega t+\theta_x^- +\varphi_x^+)}{2} \end{cases} \tag{27}$$

$$\begin{aligned} i_{Ca} &= \frac{i_{\mathrm{SMa-ac}}}{3} + \frac{i_{\mathrm{SMb-ac}}}{3} + \frac{i_{\mathrm{SMc-ac}}}{3} \\ &= I_s^- g^+ \frac{-\cos(2\omega t + \theta_x^+ + \varphi_x^-)}{2} \\ &\quad + I_s^+ g^- \frac{-\cos(2\omega t + \theta_x^+ + \varphi_x^-)}{2}. \end{aligned} \tag{28}$$

According to (28), the zero-sequence component will be left after the decoupling of ripple-power. Due to the mutual clamping effect by switched-capacitor characteristics between three-phase SM capacitors, the zero-sequence current is absorbed by the three-phase interconnected SM capacitors.

The capacitance constraint shown in (20) is under three-phase voltage symmetry condition, when the three-phase voltage asymmetry occurs, the three-phase voltage asymmetry fault ride-through simulation test waveform is shown in Fig. 21 in which the voltage of phase-b dips to 50% of the steady-state value gradually and the grid current is well controlled. In (26), the positive- and negative-sequence ripple components decouple with the SM capacitor and are canceled at the primary side of SIQAB-stage based on the three-phase symmetry.

The left zero-sequence currents, which cannot be decoupled will distribute among the three-phase SM capacitors and generate voltage ripple. The ripple degree at different dip levels is indicated in Fig. 21. When the phase-b voltage dips to 50% of the steady-state value, the capacitor voltage ripple of the SM increases from 5% to 13%, and the LVdc voltage ripple increases from 0.15% to 1.2%. Therefore, for the medium and high voltage bus connected by CHB-SIQAB, the system can realize the three-phase voltage asymmetry fault ride-through under the proposed SSHPSM method.

VI. Simulation Verification

A. Simulation Model

In order to verify the effectiveness of the SM capacitor second-order-frequency voltage ripple suppression based on the proposed SSHPSM method of HFL of CHB-SIQAB, a simulation prototype of CHB-SIQAB was built in PLECS. The specific simulation prototype parameters of the traditional large capacitance scheme and the proposed capacitance minimization schemes which are defined as Mode 1 and Mode 2, respectively, are shown in Table IV.

1) Mode 1: CHB-stage adopts the traditional control strategy shown in Fig. 3(a), QAB-stage adopts the traditional modulation method shown in Fig. 3(b) and (e). The large SM capacitance is selected as 6 mF according to (5).
2) Mode 2: CHB-stage adopts the traditional control strategy, as shown in Fig. 3(a), SIQAB-stage adopts the SSHPSM method, as shown in Fig. 5(a) and (d). The small SM capacitance is selected as 0.7 mF according to (20), which reduces by 88.3% compared with Mode 1.

B. Simulation Results

Fig. 22 is the simulation results of SM capacitor voltage of Mode 1 and Mode 2 under steady state condition. In Mode 1, the second-order-frequency voltage ripple is suppressed to 5% by large capacitance, as shown in Fig. 22(a). In Mode 2, the SM can meet the requirements of capacitor voltage ripple range by using the capacitance which is 12% of Mode 1. The voltage ripple shown in Fig. 22(b) is mainly high-frequency switching harmonic caused by SM.

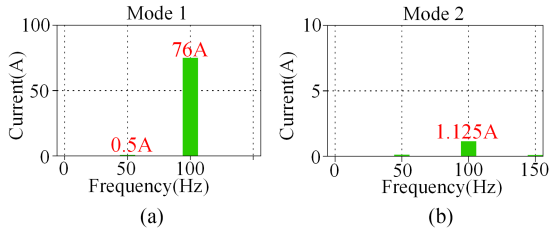

Fig. 23. FFT analysis of SM capacitor current. (a) Mode 1. (b) Mode 2.

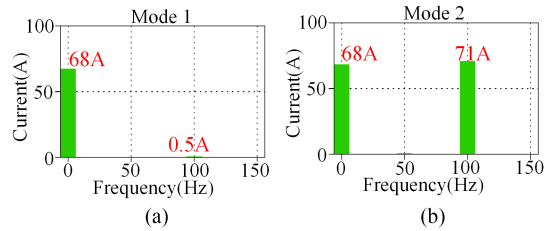

Fig. 24. FFT analysis of DC–DC-stage primary side input current. (a) Mode 1. (b) Mode 2.

Fig. 23 is the FFT decomposition results of the SM capacitor currents of the two modes. In Mode 1, the capacitor current mainly contains the second-order-frequency ripple component, while the capacitor current in Mode 2 almost does not. Fig. 24 is the FFT decomposition results of the input current of the primary side of the dc–dc-stage. In Mode 1, the QAB-stage input current hardly contains second-order-frequency ripple component, the ripple is mainly absorbed by the capacitors. In Mode 2, second-order-frequency ripple component can decouple with the three-phase SM capacitors and further flow into the primary side of SIQAB-stage to be canceled. Therefore, the capacitor only needs to deal with the high-frequency switching harmonics. The waveforms of Figs. 22–24 verify that the capacitance minimization scheme based on SSHPSM method can effectively suppress the CHB-stage SM capacitor voltage low-frequency ripple.

Fig. 25 is the HFT waveforms of SIQAB-stage of Mode 2, which verifies the correctness of the SSHPSM method shown in Fig. 5(d). The power flowing between primary and secondary sides are controlled by phase-shift modulation under SSHPSM shown in Fig. 25(a) and (b). Fig. 25(c) is the HFT currents of both primary and secondary sides. The second-order-frequency ripple component is in the form of high frequency sideband harmonics in the HFT primary side current under synchronous modulation and canceled according to magnetic coupling, therefore, the secondary side HFT current i_s only contains dc component.

Fig. 26 is the dynamic waveforms of Mode 2, Fig. 26(a) is the voltage and current of MVac grid, Fig. 26(b) is the voltage and current of LVdc bus, and Fig. 26(c) is the three-phase SM capacitor voltage. When $t = 1$ s, the load steps from full load to half load, the system with small SM capacitance can reach a stable state quickly and has good dynamic characteristics, which verifies that the optimized capacitance constraint in (20) can ensure the stable operation of CHB-SIQAB.

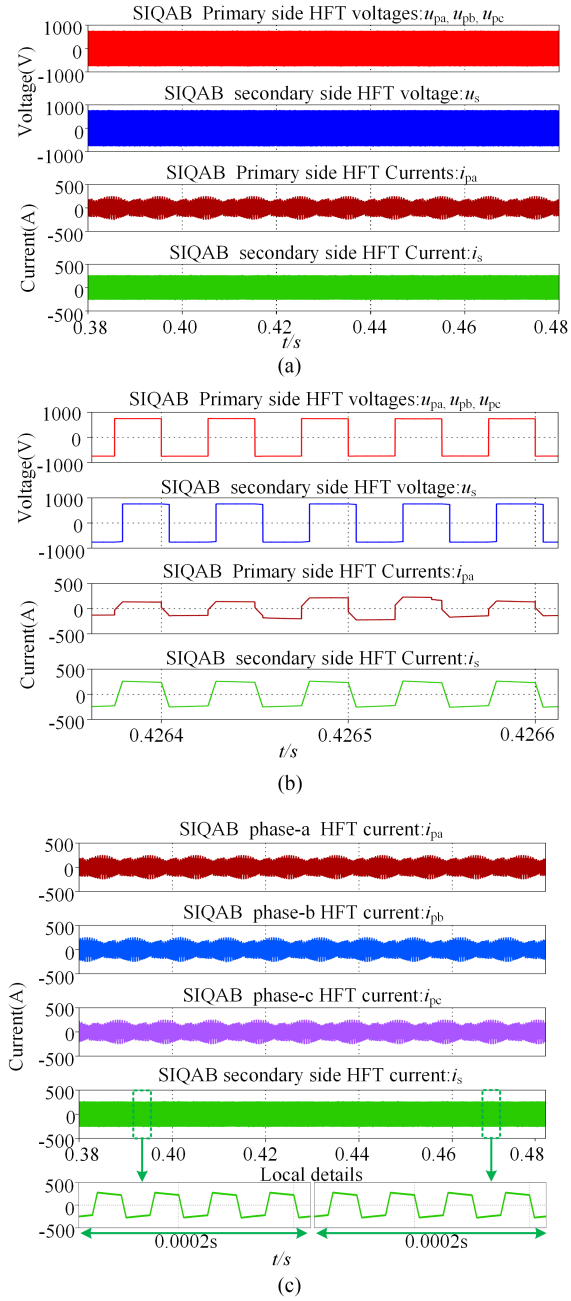

Fig. 25. Waveforms of HFT voltage and current of Mode 2. (a) Waveforms of primary and secondary sides HFT voltage and current of SIQAB-stage. (b) Local amplification. (c) Waveforms of HFT current of SIQAB-stage.

VII. Experimental Verification

In order to further verify the correctness and effectiveness of the capacitance minimization scheme based on SSHPSM and the capacitance constraint for CHB-SIQAB, a 300 W experimental prototype is built, which is shown in Fig. 27. The experimental prototype adopts three-level CHB-stage and two groups of full-bridge SIQAB-stage. The specific experimental parameters are shown in Table V, the SM capacitance is 100 uF in experiments according to (20).

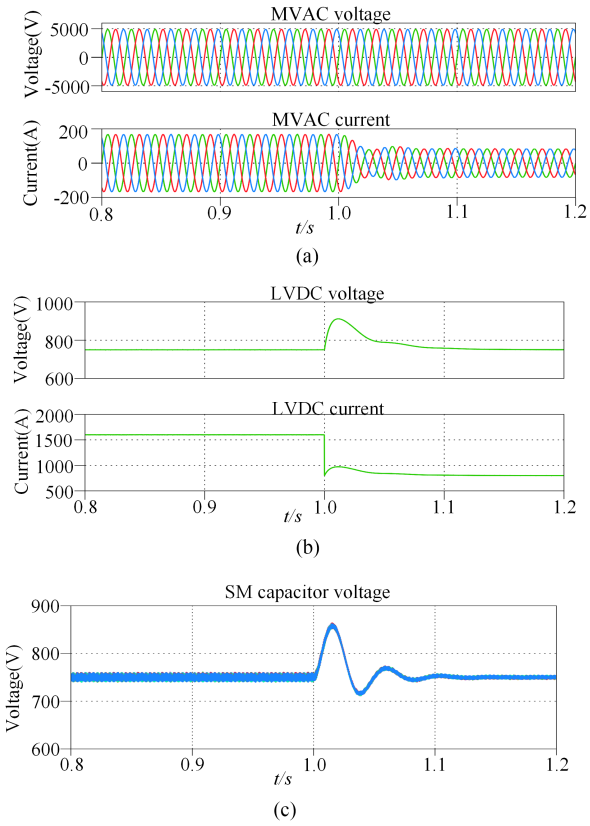

Fig. 26. Dynamic waveforms of Mode 2. (a) Waveforms of the three-phase voltage and current of the MVac gird. (b) Waveforms of the LVDC voltage and current. (c) Waveforms of the SM capacitor voltage.

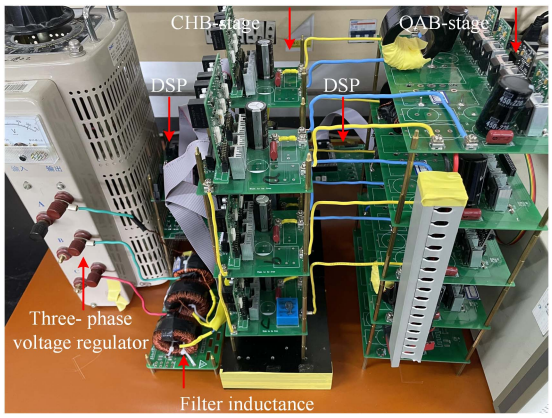

Fig. 27. CHB-SIQAB experimental prototype.

A. Ripple Suppression Verification Under Three-Phase Voltage Symmetry

Fig. 28(a) shows the phase-a current i_a of CHB-stage grid side and the SM capacitor voltage of the CHB-stage, which contains no second-order frequency ripple. Under the SSHPSM method, the second-order-frequency ripple-current will decouple with the SM capacitance and flow into the SIQAB-stage, as shown in Fig. 28(c), and the ripple-current is canceled based on the three-phase symmetry, as shown in Fig. 28(d), only

TABLE V
PARAMETERS OF EXPERIMENTAL PLATFORM

CHB-stage parameters	
SM capacitor voltage/u_C	40V
RMS value of line to line voltage/u_x	80V
Rated active power/P	300W
AC fundamental frequency/f_F	50Hz
PWM carrier frequency/f_{SM}	5kHz
SM capacitance/C	100uF
Number of SM of phase-x/n	2
QAB-stage parameters	
Transformer turns ratio/N	1:1:1:1
LVDC bus voltage/u_{LVDC}	40V
Filtering inductance/L_F	3mH
The sum of the external inductance and the equivalent leakage inductance/L_{eq}	36uH
Switching frequency of SIQAB/f_S	20kHz

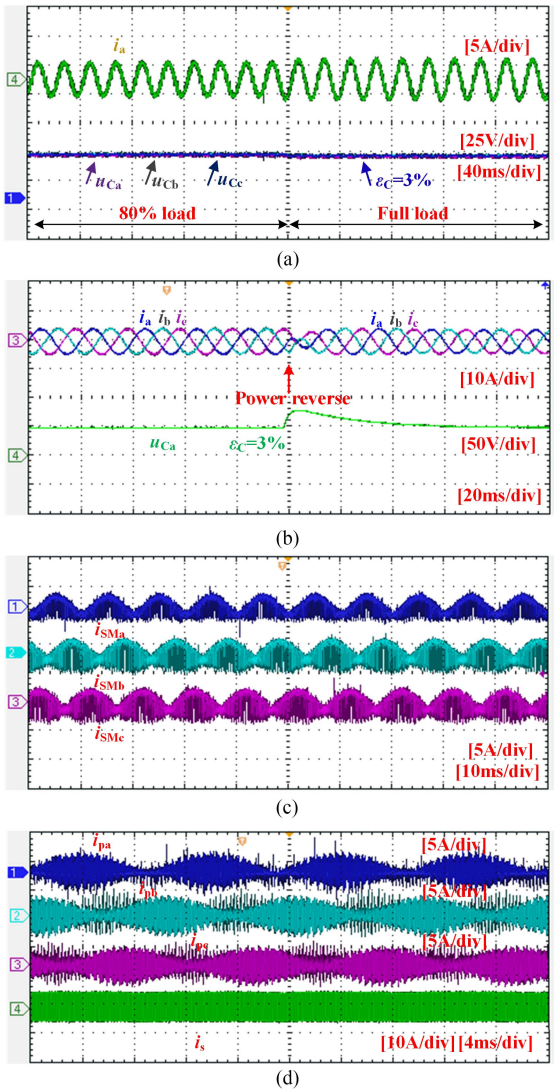

Fig. 28. Verification waveforms of SM capacitor voltage ripple suppression effect at 50 Hz. (a) Waveforms of SM capacitor voltage. (b) Waveform of the three-phase current and SM capacitor voltage when the power flow is reversed. (c) Waveforms of SIQAB-stage primary side input current. (d) Waveforms of SIQAB-stage HFT current.

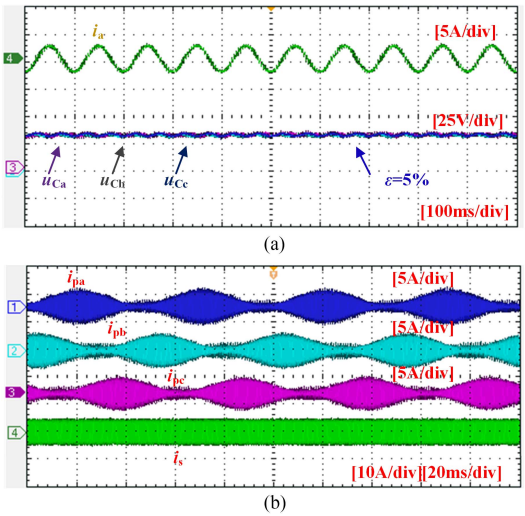

Fig. 29. Verification waveforms of SM capacitor voltage ripple suppression effect at 10 Hz. (a) Waveforms of SM capacitor voltage. (b) Waveforms of SIQAB-stage HFT current.

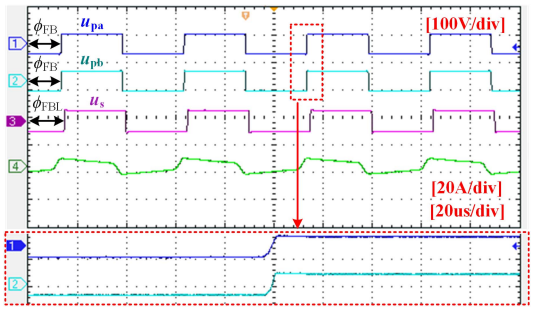

Fig. 30. Verification waveform of SSHPSM method of SIQAB-stage.

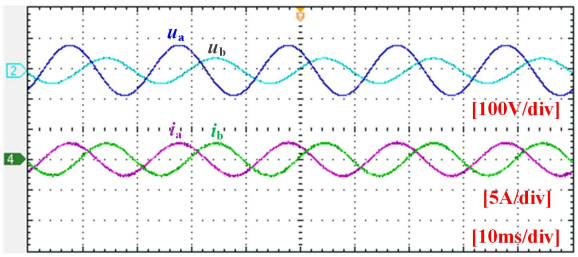

Fig. 31. Waveforms of phase-a and b voltage and current.

dc component transfer to the secondary side of SIQAB-stage. Therefore, the voltage ripple is only 3%, as shown in Fig. 28(a), and when the load is switched from 80% load to full load, the capacitor voltage ripple is still well suppressed. In addition, when the system power flow is reversed, the proposed capacitor minimization scheme can still work well, as shown in Fig. 28(b). The waveforms of Fig. 28 verify that the SM ripple-voltage suppression based on SSHPSM is effective, and the SM voltage ripple suppression process will not be affected by the dynamic change.

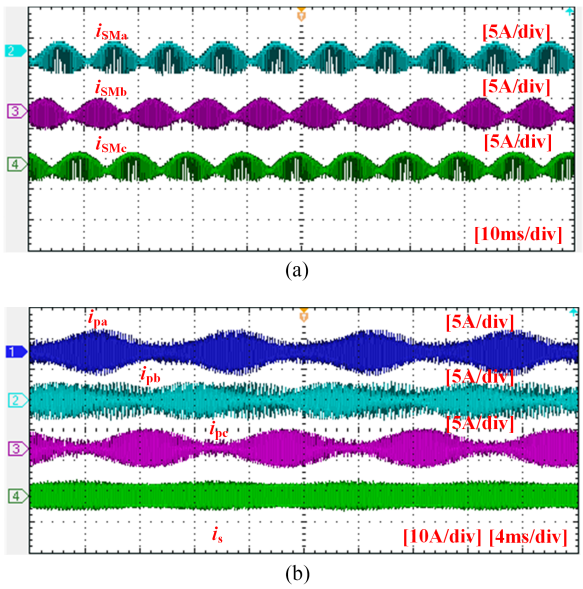

Fig. 32. Waveforms of transmitted current of SIQAB-stage under three-phase asymmetry operation. (a) Waveforms of SIQAB-stage primary side input current. (b) Waveforms of SIQAB-stage HFT current.

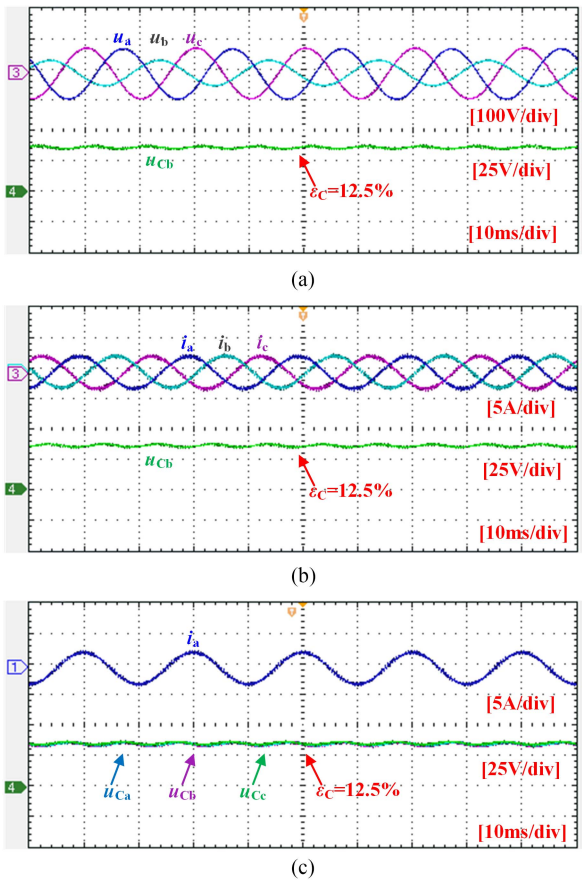

Fig. 33. Waveforms of SM capacitor voltage ripple under three-phase voltage asymmetry and current symmetry. (a) Waveforms of three-phase voltage and phase-b SM capacitor voltage. (b) Waveforms of three-phase current and phase-b SM capacitor voltage. (c) Waveforms of phase-b current and three-phase SM capacitor voltage.

As shown in Fig. 29(a), when the operating frequency of CHB-stage is 10 Hz, the SM capacitor voltage ripple of CHB-stage is 5%. Fig. 29(b) is the HFT currents. Compared with Fig. 29(c), the second-order-frequency ripple component can still be canceled in HFL, and only the dc component will transfer to the secondary side of SIQAB-stage, which verifies the effectiveness of the capacitance minimization scheme at low-frequency operation discussed in Section V-A.

Fig. 30 shows the HFT voltage and current waveforms of primary and secondary sides of SIQAB-stage, as shown in Fig. 5(d). Under synchronous modulation, the second-order-frequency ripple-current of CHB-stage SM flows into the SIQAB-stage, and the asynchronous modulation difference caused by hardware factors is very small. The power transfer is realized by the phase-shift on the primary and secondary sides of SIQAB-stage.

B. Ripple Suppression Verification Under Three-Phase Voltage Asymmetry

The three-phase voltage asymmetry condition is set as phase-b voltage dips by 50%, and the three-phase current is controlled to be symmetrical, as shown in Fig. 31.

Fig 32 is the transmitted current waveforms of SIQAB-stage under the three-phase voltage asymmetry operation. The input current of SIQAB-stage primary sides shown in (26) are given in Fig. 32(a). Fig. 32(b) shows the waveforms of HFT currents of SIQAB-stage, the positive- and negative-sequence components decouple with the SM capacitor and are canceled on the primary side of SIQAB-stage based on the three-phase symmetry, while the zero-sequence components cannot be canceled and will distribute among the three-phase interconnected capacitors.

Fig. 33 is the waveforms of SM capacitor ripple-voltage under three-phase voltage asymmetry and current symmetry. Compared with Fig. 28(a), when three-phase voltage asymmetry condition occurs, the capacitor voltage ripple increases from 3% to 12.5% due to the zero-sequence components are distributed among the three-phase capacitors, as shown in Fig. 33(c). According to Fig. 33, the proposed scheme can still suppress the SM capacitor voltage ripple in a reasonable range and realize the three-phase voltage asymmetry fault ride-through.

VIII. Conclusion

This article proposes a SM capacitance minimization strategy based on SSHPSM for CHB-SIQAB, which can reduce the capacitance of SM. Under SSHPSM, the SIQAB-stage operates in switched-capacitor mode to realize the automatic elimination of second-order-frequency voltage ripple of SM capacitor without complex control, which helps to reduce the capacitance of SM and improve the power density of the system. And the scheme is still applicable under the influence of the nonideal switch synchronization signal caused by hardware factors, and the leakage inductance inconsistency has basically no effect on the coupling progress of the ripple-currents. Furthermore, the proposed scheme can still suppress the low-frequency voltage ripple of SM capacitor in the low-frequency operation of motor drive conditions, and realize the three-phase voltage asymmetry fault ride-through for grid-tied conditions.

References

[1] Y. Yu, G. Konstantinou, B. Hredzak, and V. G. Agelidis, "Power balance of cascaded H-Bridge multilevel converters for large-scale photovoltaic integration," *IEEE Trans. Power Electron.*, vol. 31, no. 1, pp. 292–303, Jan. 2016.

[2] L. Wang, D. Zhang, Y. Wang, B. Wu, and H. S. Athab, "Power and voltage balance control of a novel three-phase solid-state transformer using multilevel cascaded H-Bridge inverters for microgrid applications," *IEEE Trans. Power Electron.*, vol. 31, no. 4, pp. 3289–3301, Apr. 2016.

[3] C. Gu, Z. Zheng, L. Xu, K. Wang, and Y. Li, "Modeling and control of a multiport power electronic transformer (PET) for electric traction applications," *IEEE Trans. Power Electron.*, vol. 31, no. 2, pp. 915–927, Feb. 2016.

[4] T. Zhao, J. Zeng, S. Bhattacharya, M. E. Baran, and A. Q. Huang, "An average model of solid state transformer for dynamic system simulation," in *Proc. IEEE Power Energy Soc. Gen. Meeting*, 2009, pp. 1–8.

[5] X. Wang, J. Liu, T. Xu, and X. Wang, "Comparisons of different three-stage three-phase cascaded modular topologies for power electronic transformer," in *Proc. IEEE Energy Convers. Congr. Expo.*, 2012, pp. 1420–1425.

[6] X. Li, L. Cheng, L. He, Z. Zhu, Y. Yang, and C. Wang, "Capacitor voltage ripple minimization of a modular three-phase AC/DC power electronics transformer with four-winding power channel," *IEEE Access*, vol. 8, pp. 119594–119608, 2020.

[7] G. Farivar, B. Hredzak, and V. G. Agelidis, "Reduced-Capacitance thin-film H-Bridge multilevel STATCOM control utilizing an analytic filtering scheme," *IEEE Trans. Ind. Electron.*, vol. 62, no. 10, pp. 6457–6468, Oct. 2015.

[8] R. Wang, F. Wang, D. Boroyevich, and P. Ning, "A high power density single phase PWM rectifier with active ripple energy storage," 2010 twenty-fifth annual," in *Proc. IEEE Appl. Power Electron. Conf. Expo.*, 2010, pp. 1378–1383.

[9] E. Rodriguez, N. Beniwal, G. Farivar, C. D. Townsend, S. Vazquez, and J. Pou, "Adaptive filtering scheme for a low-capacitance statcom," in *Proc. IEEE 4th Southern Power Electron. Conf.*, 2018, pp. 1–7.

[10] T. Isobe, D. Shiojima, K. Kato, Y. R. R. Hernandez, and R. Shimada, "Full-Bridge reactive power compensator with minimized-equipped capacitor and its application to static var compensator," *IEEE Trans. Power Electron.*, vol. 31, no. 1, pp. 224–234, Jan. 2016.

[11] Y. Hu, X. Zhang, W. Mao, T. Zhao, F. Wang, and Z. Dai, "An optimized third harmonic injection method for reducing DC-link voltage fluctuation and alleviating power imbalance of three-phase cascaded H-Bridge photovoltaic inverter," *IEEE Trans. Ind. Electron.*, vol. 67, no. 4, pp. 2488–2498, Apr. 2020.

[12] Y. Hu et al., "High-Frequency-Link current stress optimization of cascaded H-Bridge-Based solid-state transformer with third-order harmonic voltage injection," *IEEE J. Emerg. Sel. Topics Power Electron.*, vol. 9, no. 1, pp. 1027–1038, Feb. 2021.

[13] F. Xiao, C. Tu, Q. Ge, K. Zhou, Q. Guo, and Z. Lan, "Ripple voltage suppression and control strategy for CHB-Based solid-state transformer," *IEEE J. Emerg. Sel. Topics Power Electron.*, vol. 9, no. 1, pp. 1104–1118, Feb. 2021.

[14] G. Gohil, H. Wang, M. Liserre, T. Kerekes, R. Teodorescu, and F. Blaabjerg, "Reduction of DC-link capacitor in case of cascade multilevel converters by means of reactive power control," in *Proc. IEEE Appl. Power Electron. Conf. Expo.*, 2014, pp. 231–238.

[15] T. Isobe, R. A. Barrera-Cardenas, Z. He, Y. Zou, K. Terazono, and H. Tadano, "Control of three-phase solid-state transformer with phase-separated configuration for minimized energy storage capacitors," *IEEE J. Emerg. Sel. Topics Power Electron.*, vol. 8, no. 3, pp. 3014–3028, Sep. 2020.

[16] L. F. Costa, G. Buticchi, and M. Liserre, "Modular smart transformer architectures: An overview and proposal of a interphase architecture," in *Proc. IEEE 8th Int. Symp. Power Electron. Distrib. Gener. Syst.*, 2017, pp. 1–7.

[17] K. Wang, M. Andresen, Y. Ko, and M. Liserre, "Cascaded multilevel topology based on quadruple active bridges for phase power balancing in Large-scale PV systems," in *Proc. IEEE 21st Eur. Conf. Power Electron. Appl.*, 2019, pp. P.1–P.8.

[18] T. Liu et al., "High-Efficiency control strategy for 10-kV/1-MW solid-state transformer in PV application," *IEEE Trans. Power Electron.*, vol. 35, no. 11, pp. 11770–11782, Nov. 2020.
[19] M. Feng, C. Gao, J. Ding, H. Ding, J. Xu, and C. Zhao, "Hierarchical modeling scheme for high-speed electromagnetic transient simulations of power electronic transformers," *IEEE Trans. Power Electron.*, vol. 36, no. 9, pp. 9994–10004, Sep. 2021.
[20] [Online]. Available: https://www.infineon.com/dgdl/Infineon-FF6MR12KM1-DataSheet-v02_00-EN.pdf?fileId=5546d46272aa54c00172bcb72b5e56bc
[21] [Online]. Available: https://www.infineon.com/dgdl/Infineon-FF3MR12KM1-DataSheet-v02_00-EN.pdf?fileId=5546d46272aa54c00172bc9c15f5569e
[22] [Online]. Available: https://www.infineon.com/dgdl/Infineon-FF2MR12KM1-DataSheet-v02_00-EN.pdf?fileId=5546d46272aa54c00172bc9bf70c569b
[23] Z. Guo, R. Yu, W. Xu, X. Feng, and A. Q. Huang, "Design and optimization of a 200-kW medium-frequency transformer for medium-voltage SiC PV inverters," *IEEE Trans. Power Electron.*, vol. 36, no. 9, pp. 10548–10560, Sep. 2021.
[24] M. A. Bahmani and T. Thiringer, "Accurate evaluation of leakage inductance in high-frequency transformers using an improved frequency-dependent expression," *IEEE Trans. Power Electron.*, vol. 30, no. 10, pp. 5738–5745, Oct. 2015.
[25] M. Amiri, M. Feyzi, and H. Saberi, "A modified torque control approach for load sharing application using V/F induction motor drives," in *Proc. IEEE 4th Annu. Int. Power Electron., Drive Syst. Technol. Conf.*, 2013, pp. 1–6.
[26] S. Zhao, J. Liu, and S. Du, "Capacitance minimization for a medium-voltage motor drive based on cascaded H-Bridges," in *Proc. IEEE 4th Int. Conf. HVdc*, 2020, pp. 531–536.

Yuzhuo Pan received the B.S. degree in 2019 from the Yanshan University, Qinhuangdao, China, where he is currently working toward the Ph.D. degree all in electrical engineering.

His current research interests include modular multilevel converter and multiport power router.

Jiaxun Teng received the B.S. degree in electrical engineering from Harbin Institute of Technology, Weihai, China, in 2017, and the M.S. degree in power electronics in 2021 from Yanshan University, Qinhuangdao, China, where he is currently working toward the Ph.D. degree in artificial intelligence.

He has been with the Key Laboratory of Power Electronics for Energy Conservation and Motor Drive of Hebei Province since 2021. His current research interests include circuit topology, analysis and control of modular multilevel converter-based medium and high-voltage direct current systems, multibus multiport energy router, medium-voltage motor drive, and power electronics transformer.

Chen Yang received the B.S. degree in 2020 from the Yanshan University, Qinhuangdao, China, where he is currently working toward the M.S. degree all in electrical engineering.

Her current research interests include modular multilevel converter and multiport power router.

Zemin Bu received the B.S. degree from the Shanxi Institute of Technology, Yangquan, China, in 2018. He is currently working toward the Ph.D. degree with Yanshan University, Qinhuangdao, China, all in electrical engineering.

His current research interests include modular multilevel converter and solid-state transformer.

Baocheng Wang received the B.S. and M.S. degrees from Northeast Heavy Machinery Institute, Fulaerhchi, China, in 1988 and 1991, respectively, and the Ph.D. degree from Yanshan University, Qinhuangdao, China, in 2008, all in electrical engineering.

Since 2005, he has been a Professor with the Department of Electrical Engineering, Yanshan University. His research interests include power conversion and renewable energy systems.

Xin Li received the B.Eng. degree in computer software and applications from Northeast Heavy Machinery College, Yanshan University, Qinhuangdao, China, in 1992, and the M.Eng. degree in measurement technique and automation equipment and the Ph.D. degree in measurement technology and instruments from Yanshan University, in 2002 and 2008, respectively.

Her current research interests include power electronics, intelligent information processing, bioinformatics, and biomedical instruments.

Xiaofeng Sun (Member, IEEE) received the B.S. degree in electrical engineering from Northeast Heavy Machinery Institute, Heilongjiang, China, in 1993, and the M.S. and Ph.D. degrees in power electronics from Yanshan University, Qinhuangdao, China, in 1999 and 2005, respectively.

From 2003 to 2007, he was an Associate Professor with Yanshan University, where he has been a Professor since 2008. He is also the Director with the Key Laboratory of Power Electronics for Energy Conservation and Motor Drive of Hebei Province. He has authored or coauthored more than 70 transactions and conference papers. His research interests include dc–dc converters, multiple-input converters, hybrid electric vehicles, microgrids, and power quality control.